



| | |
|--------------|---|
| Title | Porous carbon derived from biomass and polymer for high performance supercapacitors |
| Author(s) | 舒, 羽 |
| Citation | 大阪大学, 2017, 博士論文 |
| Version Type | VoR |
| URL | https://doi.org/10.18910/69241 |
| rights | |
| Note | |

The University of Osaka Institutional Knowledge Archive : OUKA

<https://ir.library.osaka-u.ac.jp/>

The University of Osaka

Doctoral Dissertation

**Porous carbon derived from biomass and polymer for
high performance supercapacitors**

バイオマスとポリマーを由来とする高性能スーパー
キャパシター用多孔質炭素の開発

Yu Shu

August 2017

Graduate School of Engineering

Osaka University

Contents

| | Page |
|---|------|
| General introduction | 1 |
| References | 11 |
| | |
| Chapter 1 | |
| | |
| Hierarchical activated green carbons from abundant biomass waste for symmetric supercapacitors | |
| 1.1 Introduction | 16 |
| 1.2 Experimental | 17 |
| 1.3 Results and discussion | 20 |
| 1.4 Conclusion | 30 |
| 1.5 References | 31 |
| | |
| Chapter 2 | |
| | |
| Fabrication of N-doped and shape-controlled porous monolithic carbons from polyacrylonitrile for supercapacitors | |
| 2.1 Introduction | 33 |
| 2.2 Experimental | 33 |
| 2.3 Results and discussion | 36 |
| 2.4 Conclusion | 50 |
| 2.5 References | 50 |

Chapter 3

Novel porous carbon from biomass/polymer composite for high performance supercapacitor

| | |
|----------------------------|----|
| 3.1 Introduction | 53 |
| 3.2 Experimental | 54 |
| 3.3 Results and discussion | 56 |
| 3.4 Conclusion | 68 |
| 3.5 References | 69 |

| | |
|---------------------------|----|
| Concluding remarks | 71 |
|---------------------------|----|

| | |
|-----------------------------|----|
| List of publications | 73 |
|-----------------------------|----|

| | |
|------------------------|----|
| Acknowledgments | 75 |
|------------------------|----|

General introduction

The current issues we faced including the growing energy demands, continuous depletion of fossil fuels, and climate change impel the whole society to move towards alternative low-cost, environmental friend, and sustainable energy sources, as well as energy conversion and storage technologies.¹⁻³ Supercapacitors (SCs), also called as ultracapacitors or electrochemical capacitors, have increasingly emerged and attracted significant attention as an alternative electrical energy storage device due to their high power density (10 kW kg^{-1}), rapid charge/discharge process (within seconds or less), long cycle life (> 10000 cycles), low self-discharging, safe operation, and low cost in comparison to other batteries.^{4, 5} The range of commercial large-scale applications of SCs technology is gradually expanding. To date, they have been applied in electric bus, metro trains, hybrid energy-efficient forklift, off-shore variable speed wind turbines, and electric ferry.⁶⁻⁸ Thus, SCs play a more and more important role in achieving the growing energy demands, reducing the reliance on petroleum sources, and decreasing harmful emissions. The development on high performance SCs is highly desired for current society.

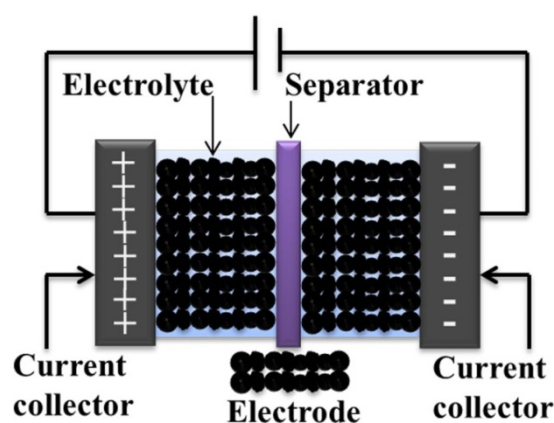


Figure 1. Scheme of a typically symmetrical SC based on porous electrode materials.

As shown in Fig. 1, a typical supercapacitor corresponding to porous carbon materials consists of an electrolyte, two electrodes, a separator that electrically isolates the two electrodes, and two current collectors. In principle, SCs can be broadly

classified into two main categories based on the distinct charge storage mechanisms (Fig. 2), namely: i) the electrical double-layer (EDL) capacitor and ii) the pseudo-capacitor.⁹⁻¹¹ The capacitance in the former comes from plentiful charges accumulated in the electrode/electrolyte interface (Fig. 3). By contrast, pseudo-capacitance arises from reversible oxidation/reduction (redox) or the Faradaic charge transfer reactions between the electrolyte ions and active species on the surface of electrodes.¹² Although higher capacitance can be achieved by pseudo-capacitor than EDL capacitor, pseudo-capacitor often suffers from the poor electrical conductivity of the active species, resulting in low power density and cycling stability.¹³ Therefore, the combination of EDL- and pseudo-capacitance presents an effective approach to improve the overall capacitance of SCs.

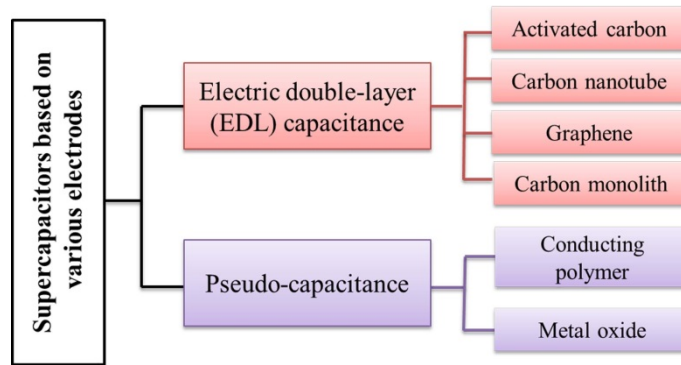


Figure 2. Types of SCs classified by their charge storage mechanisms and the adopted electrode materials.

The overall performance of SCs is determined by the properties of the employed electrolyte and electrode. Electrolytes used in SCs are usually aqueous, organic, or liquid salts. The electrochemical stability window and ionic conductivity are the two main criteria for selection of an electrolyte. The stability window is important to maximize the energy density of SCs, while the ionic conductivity has a major influence on the values of power density of SCs.⁵ A series of electrochemical measurements must be carried out to evaluate the performance of SCs and to identify their specific capacitance, specific power, and energy density. The electrochemical performance of

SCs can be analyzed by cyclic voltammetry (CV), galvanostatic charge/discharge (GC) techniques, and electrochemical impedance spectroscopy (EIS).

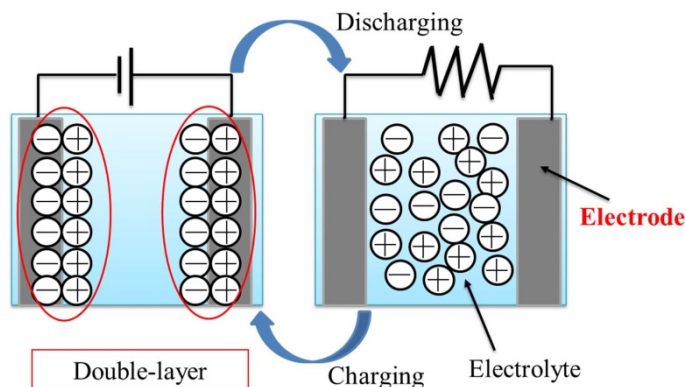


Figure 3. Schematic illustration of the charging/discharging process in SCs.

Electrode, as the heart of SCs, is the most important component which determines the electrochemical properties of SCs in terms of self-discharge, capacity, resistance, life-expectancy, and so on.¹⁴ Electrode materials for SCs can be categorized into three types including carbon-based materials with high specific surface area, conducting polymers (CPs), and metal oxides (Fig. 2).¹⁵ Among them, conducting polymers usually generate capacitance behavior through the redox process.¹⁶ The commonly CPs used in SCs are polyaniline, polypyrrole, poly(p-phenylene vinylene), polythiophene, and their derivatives.¹⁷⁻¹⁹ Although these polymers show the merits of low environmental impact, adjustable redox activity, and high storage capacity, the shortages of strict potential window and low cycling stability are still serious problems for the large-scale applications in SCs.⁹ Comparatively, metal oxides can give rise to higher energy density than conventional carbon-based materials, and better stability than CPs because they not only store charges by electrostatic process but also support the Faradaic reactions between the electrodes and electrolyte ions.⁹ However, the high cost of precious metals such as ruthenium (Ru) is a major disadvantage for commercial applications of RuO₂-based SCs.

In the recent few decades, carbon materials are regarded as the most promising electrode materials for SCs industrialization because of the advantages of abundance,

relatively low cost, easy processing, non-toxicity, high specific surface area, wide operating temperature range, good electronic conductivity, and high chemical stability.²⁰⁻²² Thus, this thesis has been done focusing on the development of porous carbons as SCs electrode materials. In Fig. 2, some examples of carbon materials that can be used in SCs are given, including activated carbon (AC), carbon nanotubes (CNTs), graphene, and carbon monolith.²³⁻²⁶ Normally, carbon-based SCs are close to a mechanism of electric double-layer capacitance. The capacitance mainly relies on the surface area accessible to electrolyte ions. The significant factors influencing the electrochemical performance are specific surface area, pore size distribution, and electrical conductivity of the carbon materials.

In general, carbon materials with higher surface area display a larger capability for charge accumulated at the interface of electrode/electrolyte. However, the specific surface area of carbon materials is sometimes not directly proportional to the specific capacitance of SCs, which is attributed to that not all pores in the electrode layer can necessarily accept electrolyte ions.^{6, 12}

Recently, carbon materials with hierarchical porous structure display even superior supercapacitor performance, especially at high current rates, since their unique structures provide critical features required for the high-performance electrodes.²⁷⁻²⁹ Abundant micropores (<2 nm) offer large surface areas for formation of electric double-layers to enhance the possible electrostatic adsorption area; plentiful mesopores (2~50 nm) provide the low-resistance pathway for ions to be transported to electrode/electrolyte interfaces, and macropores (>50 nm) existed in electrodes act as ion-buffering reservoirs to ensure the electrolyte ion transportation at high rates.³⁰ It has been found that electrolyte ions are inaccessible to too small pore sizes (<0.5 nm), and micropores with closed structures or narrow bottleneck morphologies often hinder ion transportation.³¹ In fact, an appropriate proportion of micropore to mesopore is beneficial to both the energy density and power density of SCs. Besides, compatibility between the pore sizes and ion diameters is also important for SCs. Therefore, synthesis

of hierarchical porous carbons through a facile process is of great significance in developing outstanding energy storage systems.

In addition to large surface area and proper pore size distribution, the surface heteroatoms of carbon materials have also been considered an effective way to improve the specific capacitance by contributing additional pseudo-capacitance through the Faradaic reactions.³¹⁻³⁴ Heteroatoms providing a pair of electrons can significantly enhance the electrical conductivity, adjust the electron donor/acceptor properties of carbon materials, and consequently maximize the electroactive surface area, which accordingly gives rise to a pseudo-capacitive reaction.^{35,36} Thus, the major challenge for the development of carbon-based electrode materials for high performance SCs is how to achieve carbons possessing desirable properties including large surface area, efficient porosities, high conductivity, and moderate surface functionality.

As a promising method to improve the capacitive performance, the introduction of heteroatoms, such as B, O, P, N, or S, into carbon frameworks has attracted considerable attention in recent years.³⁷⁻⁴⁰ For instance, the oxygen-containing functionalities can contribute the electron-acceptor properties into the carbon surface; phosphorus can promote the charge delocalization of carbon atoms and then lead to a carbon morphology with open edged sites; boron atoms in a carbon lattice can give rise to oxidation resistance and modify the electronic structure of carbon; nitrogen atoms can enhance electrical conductivity and electrochemical activity. Furthermore, heteroatoms-containing functionalities can improve the wettability between electrode materials and aqueous electrolytes, resulting in an increased accessible surface area for electrolyte.

Among the heteroatoms mentioned, the introduction of nitrogen has been extensively investigated for SCs applications over the past few years and it is proved to be positive in modifying the wettability of electrodes and improving the electrical conductivity and capacitive performance.^{34, 35} In general, four types of the doped nitrogen in carbons, depending on the bonding environments, include pyrrolic/pyridonic

N (N-5), pyridinic N (N-6), quaternary N (N-Q), and N oxides of pyridinic N (N-X).⁴¹ Among them, N-5 and N-6 contribute to the pseudo-capacitance, while N-Q and N-X promote electron transport.⁴²

Traditional N-doped carbons are usually prepared by introducing a certain amount of nitrogen into carbon frameworks *via* a post-treatment process, such as treat with ammonia, urea, amines, etc; however, the content of introduced nitrogen is relatively low and the formed nitrogen-containing functional groups are usually unstable.⁴³⁻⁴⁵ In contrast, due to the easy and facile process, the method of directly employing N-enriched precursors, such as polyaniline (PANI), polypyrrole (PPy), polyacrylonitrile (PAN), polybenzoxazine (PBZ), melamine, dicyandiamide and cyanamide, seems to be a promising approach to prepare N-doped carbon materials.⁴⁶⁻⁴⁹ Moreover, the nitrogen species and nitrogen content can be tailored by controlling the synthetic conditions of N-doped carbon materials. Another way to increase the capacitance is to introduce conducting polymers or metal oxides into the carbon materials for the formation of carbon composite, which offers both physical and chemical charge storage mechanism together in a single electrode.⁵⁰⁻⁵²

According to the above discussion, N-enriched hierarchically porous carbons can be the optimum candidates for SCs application to optimize the overall capacitance and conductivity of the electrodes without destroying the electrochemical stability and high rate property. Thus, the study on N-doped hierarchically porous carbons has aroused extremely great interest in the field of energy storage.

To date, hierarchical porous carbons are widely investigated by combining hard-template or soft-template approach and post-activation method. However, most of the templates are expensive and the removal process of the template is usually complicated, time-consuming, and harmful to environment. As a consequence, developing an efficient and eco-friendly synthetic strategy without template for hierarchical carbons is of great significance.

It is well known that the porosity and capacitance of porous carbon materials

can be generally balanced by adjusting the conditions of pyrolysis process.⁵³⁻⁵⁵ Two main activation methods are physical and chemical treatments. The physical activation process refers to the use of gasifying agents such as steam, carbon dioxide, or mixed gases at a high temperature (700-1200 °C) to create porosity in carbonaceous precursors. On the other hand, in a chemical treatment, the precursor is impregnated by chemical agent and then activated at a relatively low temperature (usually 600-900 °C) under an inert atmosphere.⁵⁶ Chemical agents basically act as dehydrating agents and oxidants, which could influence the pyrolytic decomposition and prevent the formation of the tar or ash during the activation process. The used chemical agents usually include KOH, K₂CO₃, H₃PO₄, or ZnCl₂.⁵⁷⁻⁵⁹ The chemical treatment is more commonly used due to the low energy consumption, well-developed pores, high yield, and low cost. Since both the specific surface area and pore size distribution of the final carbons have a great impact on the capacitive behavior when they are employed as electrodes, the ability of adjusting the pore characters of carbons will allow one to improve the performance of carbon-based SCs.

In addition, the employed precursors play a primary role in influencing the qualities and characteristics of the resulting carbons. Basically, carbonaceous materials possessing inherent porosity, filterability, and high carbon content could be used as the starting materials for the preparation of carbon materials.⁶⁰⁻⁶² Considering a long-term perspective of sustainable development and environment protection, it is essential and highly desirable to look for renewable natural resources along with develop facile but economical synthetic methods for the practical application of carbon materials in the energy storage.

Towards this direction, biomasses, naturally abundant and renewable resources, have become popular for the production of functional porous carbon materials due to their low cost, eco-friendliness, and easy fabrication. Biomass-derived porous carbons, such as from palm shell, cherry stones, ramie, pomelo peel, corncob residue, have already been reported.⁶³⁻⁶⁷ These also showed great potential as electrode materials for

SCs. Although many kinds of biomass resources have been employed to prepare porous carbons, it is still an urgent to search for cheap and accessible precursors to create significant economic valorization.

Amygdalus pedunculata Pall., a member of the family Rosaceae, is a type of sand dune-stabilizing and oil-bearing shrubs. Its high tolerance and adaptability to a wide range of soil types and moisture conditions make it as a good candidate for desert reclamation and landscaping plants on roadsides. Using *Amygdalus pedunculata* as renewable resources for common and functional products is highly significant for desert greening as well as economic development in the desert area. The kernel with high fatty acid content has been used to prepare edible oil, biodiesel, and protein.⁶⁸⁻⁷⁰ The fruit yield is around 6000 kg ha⁻¹ per year at peak time with 70–80% *Amygdalus pedunculata* shell (APS) by weight. APS is rich in carbon, and possesses significant mechanical strength and low ash content besides being abundant in nature and less-costly; therefore, APS can be regarded as a kind of novel starting material for production of hierarchically porous carbons for SCs. As shown in Fig. 4, hierarchical porous AC was obtained by a nontoxic K₂CO₃ activation method and applied for SC electrode. The development of APS would promote the connection between desert reclamation and green energy storage.

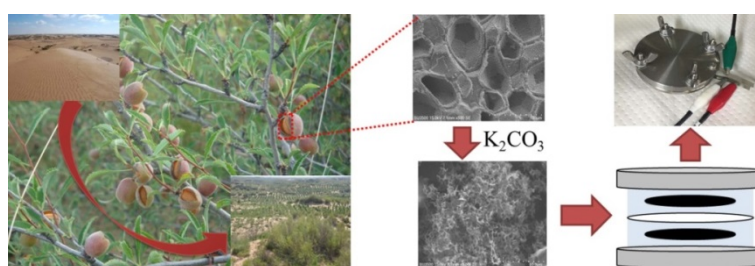


Figure 4. Hierarchical porous AC derived from *Amygdalus pedunculata* shell (APS) and the electrochemical application on SCs.

Apricot is known as one of the most favorite fruits worldwide. The world production apricot is about 3.5 million tons according to the report of FAOSTAT and the shells occupy 6% of the total fruit production. Tons of apricot shell (AS), the

by-product of apricot, are formed and most of them are abandoned, polluting the environment by the incinerating or uncontrolled decomposition. As a kind of lignocellulosic biomass, AS mainly consists of cellulose, hemicellulose, and lignin, which also can be transformed into porous carbons by calcining at a high temperature.⁷¹

On the other hand, directly pyrolysis of nitrogen-containing polymers seems to be an effective approach to prepare N-doped porous carbons. Polyacrylonitrile (PAN), a widely used precursor for synthesizing carbon materials, possesses a nitrogen atom per monomeric unit and forms a stable ladder structure after cyclization reaction to withstand the further high temperature.^{72, 73} However, most studies of PAN-based carbons focused on the preparation of carbon fibers.⁷⁴⁻⁷⁶ Limited reports were to prepare activated porous carbons or monolithic carbons through an easy pyrolysis process.

In Uyama's group the author belongs to, three-dimensional (3D) polymer-based monoliths have been fabricated by a template-free thermally induced phase separation (TIPS) technique.⁷⁷⁻⁸⁰ The typical procedure of the TIPS approach is as follows. Polymers are firstly dissolved in an appropriate solvent by heating, followed by cooling the solution. During the cooling step, the phase separation of the polymer solution takes place to form the 3D porous monoliths without any templates. The shape of the monoliths can be designed by the vessels used during the phase separation process. PAN monolith and it-derived carbon were first published using TIPS method followed by a pyrolysis process.⁸¹ The microstructure of the prepared activated carbon monolith was restored even after heating at a high temperature. This activated carbon monolith interestingly possessed high adsorption capacity for carbon dioxide. Considering the merits of TIPS and PAN and the requirements of electrode materials, it is highly promising to develop porous carbons of high surface area, nitrogen self-doped, and controllable shape to high performance SCs.

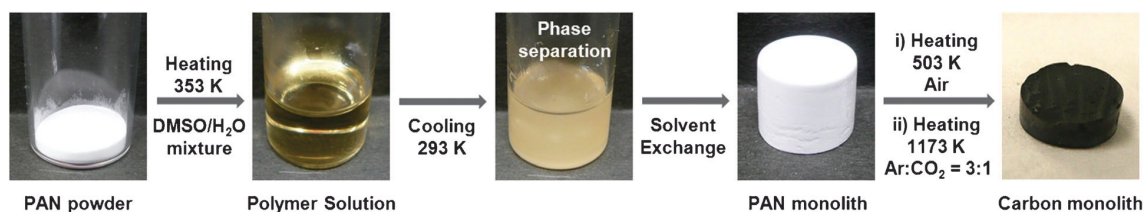


Figure 5. A general protocol for preparation of mesoporous PAN and activated carbon monoliths by a thermally induced phase separation technique.⁸⁰

Based on the background described above, this thesis focuses on the preparation of porous carbons from biomass and polymer and their applications on SCs electrodes. First, hierarchical ACs were prepared from biomass wastes including APS and AS. Then, N-doped and shape-controlled monolithic carbons were fabricated from PAN *via* a template-free TIPS approach followed by a pyrolysis process. Finally, the composite porous carbon derived from AS-based AC (ASAC) and PAN was obtained. The excellent performance of the composite carbon was expected to be achieved by combination of the advantages of hierarchical structure of ASAC and high N content of PAN. This thesis is composed of three chapters.

In Chapter 1, the preparation of hierarchical ACs derived from AS and their application on SCs are described. According to adjusting the activation time and activation temperature, a series of ACs with different specific surface areas and porosity parameters was obtained. The effects of the activation time and temperature on the specific surface area and porosity were explored systematically. The electrochemical performances of the obtained ACs were fully evaluated on an assembled AC//AC symmetrical SC system by cyclic voltammetry (CV) and galvanostatic constant current charge/discharge (GC) measurements.

In Chapter 2, the author discusses the fabrication of N-doped porous monolithic carbons (PMC) from PAN by the low-cost and facile template-free TIPS approach followed by a pyrolysis process. The obtained PAN monolith, as the precursor to prepare carbons, showed a three-dimensional (3D) porous structure and its shape can be designed during the phase separation step which will be beneficial to give the further product carbon a controllable shape. In addition, two typical pyrolysis methods

including carbon dioxide and potassium hydroxide activation were employed and compared to obtain the PMC with desired properties. The specific surface areas and porosity parameters were systematically investigated and the electrochemical performances were fully evaluated on both three- and two-electrode systems. In comparison with the carbon prepared by CO₂ activation (CD-PMC), porous monolithic carbon activated by KOH method (PMC) possessed a large surface area, suitable pore size distribution, and high N content, resulting in a more excellent electrochemical performance on SC applications.

In Chapter 3, the development of N-doped porous monolithic carbon (NDPMC) from ASAC/PAN composite is described. A template-free TIPS approach followed by KOH activation was employed to obtain NDPMC. The composite monolith displayed a high weight residue and large specific surface area than that of the pure PAN monolith (Chapter 2). The electrochemical results showed that NDPMC with large surface area and high nitrogen content exhibited high specific capacitance, outstanding rate capability, and excellent cycle stability, demonstrating that NDPMC is a highly promising candidate for high performance SC.

References

1. S. Chu and A. Majumdar, *Nature*, 2012, **488**, 294-303.
2. P. Simon and Y. Gogotsi, *Nat. Mater.*, 2008, **7**, 845-854.
3. T. Sheng, Y. F. Xu, Y. X. Jiang, L. Huang, N. Tian, Z. Y. Zhou, I. Broadwell and S. G. Sun, *Acc. Chem. Res.*, 2016, **49**, 2569-2577.
4. H. Jiang, P. S. Lee and C. Li, *Energy Environ. Sci.*, 2013, **6**, 41-53.
5. F. Beguin, V. Presser, A. Balducci and E. Frackowiak, *Adv. Mater.*, 2014, **26**, 2219-2251.
6. L. L. Zhang and X. S. Zhao, *Chem. Soc. Rev.*, 2009, **38**, 2520-2531.
7. H. Jiang, L. Yang, C. Li, C. Yan, P. S. Lee and J. Ma, *Energy Environ. Sci.*, 2011, **4**, 1813-1819.

8. W. Gu and G. Yushin, *WIREs Energy Environ.*, 2014, **3**, 424-473.
9. G. Wang, L. Zhang and J. Zhang, *Chem. Soc. Rev.*, 2012, **41**, 797-828.
10. Z. S. Iro, C. Subramani and S. S. Dash, *Int. J. Electrochem. Sci.*, 2016, **11**, 10628-10643.
11. E. Frackowiak, G. Lota, J. Machnikowski, C. Vix-Guterl and F. Béguin, *Electrochim. Acta*, 2006, **51**, 2209-2214.
12. Z. Yu, L. Tetard, L. Zhai and J. Thomas, *Energy Environ. Sci.*, 2015, **8**, 702-730.
13. T. Chen and L. Dai, *Materials Today*, 2013, **16**, 272-280.
14. S. M. Chen, R. Ramachandran, V. Mani, R. Saraswathi, *Int. J. Electrochem. Sci.*, 2014, **9**, 4072-4085.
15. E. Frackowiak, *Phys. Chem. Chem. Phys.*, 2007, **9**, 1774-1785.
16. A. M. Bryan, L. M. Santino, Y. Lu, S. Acharya and J. M. D'Arcy, *Chem. Mater.*, 2016, **28**, 5989-5998.
17. Y. Xu, Y. Tao, X. Zheng, H. Ma, J. Luo, F. Kang and Q. H. Yang, *Adv. Mater.*, 2015, **27**, 8082-8087.
18. G. Xiong, C. Meng, R. G. Reifengerger, P. P. Irazoqui and T. S. Fisher, *Adv. Energy Mater.*, 2014, **4**, 1300515.
19. V. Khomenko, E. Frackowiak and F. Béguin, *Electrochim. Acta*, 2005, **50**, 2499-2506.
20. Y. Zhai, Y. Dou, D. Zhao, P. F. Fulvio, R. T. Mayes and S. Dai, *Adv. Mater.*, 2011, **23**, 4828-4850.
21. S. Dutta, A. Bhaumik and K. C. W. Wu, *Energy Environ. Sci.*, 2014, **7**, 3574-3592.
22. K. Shi, M. Ren and I. Zhitomirsky, *ACS Sustainable Chem. Eng.*, 2014, **2**, 1289-1298.
23. X. Gao, W. Xing, J. Zhou, G. Wang, S. Zhuo, Z. Liu, Q. Xue and Z. Yan, *Electrochim. Acta*, 2014, **133**, 459-466.
24. I. M. De la Fuente Salas, Y. N. Sudhakar and M. Selvakumar, *Appl. Surf. Sci.*, 2014, **296**, 195-203.
25. L. Wang, G. Mu, C. Tian, L. Sun, W. Zhou, P. Yu, J. Yin and H. Fu, *ChemSusChem*, 2013, **6**, 880-889.
26. P. Simon and Y. Gogotsi, *Acc. Chem. Res.*, 2013, **46**, 1094-1103.
27. C. Z. Yuan, B. Gao, L. F. Shen, S. D. Yang, L. Hao, X. J. Lu, F. Zhang, L. J. Zhang

- and X. G. Zhang, *Nanoscale*, 2011, **3**, 529-545.
28. L. Estevez, R. Dua, N. Bhandari, A. Ramanujapuram, P. Wang and E. P. Giannelis, *Energy Environ. Sci.*, 2013, **6**, 1785-1790.
 29. L. Qie, W. Chen, H. Xu, X. Xiong, Y. Jiang, F. Zou, X. Hu, Y. Xin, Z. Zhang and Y. Huang, *Energy Environ. Sci.*, 2013, **6**, 2497-2504.
 30. H. C. Huang, C. W. Huang, C. T. Hsieh and H. Teng, *J. Mater. Chem. A*, 2014, **2**, 14963-14972.
 31. Q. Wang, J. Yan and Z. Fan, *Energy Environ. Sci.*, 2016, **9**, 729-762.
 32. Y. Li, X. Xu, Y. He, Y. Jiang and K. Lin, *Polymers*, 2017, **9**, 2.
 33. K. Yan, L. B. Kong, K. W. Shen, Y. H. Dai, M. Shi, B. Hu, Y. C. Luo and L. Kang, *Appl. Surf. Sci.*, 2016, **364**, 850-861.
 34. X. Tong, H. Zhuo, S. Wang, L. Zhong, Y. Hu, X. Peng, W. Zhou and R. Sun, *RSC Adv.*, 2016, **6**, 34261-34270.
 35. Y. Deng, Y. Xie, K. Zou and X. Ji, *J. Mater. Chem. A*, 2016, **4**, 1144-1173.
 36. K. A. Cychosz, R. Guillet-Nicolas, J. Garcia-Martinez and M. Thommes, *Chem. Soc. Rev.*, 2017, **46**, 389-414.
 37. H. Chen, D. Liu, Z. Shen, B. Bao, S. Zhao and L. Wu, *Electrochim. Acta*, 2015, **180**, 241-251.
 38. Z. Q. Zhao, P. W. Xiao, L. Zhao, Y. Liu and B. H. Han, *RSC Adv.*, 2015, **5**, 73980-73988.
 39. L. Zhou, H. Cao, S. Zhu, L. Hou and C. Yuan, *Green Chem.*, 2015, **17**, 2373-2382.
 40. J. Patiño, N. López-Salas, M. C. Gutiérrez, D. Carriazo, M. L. Ferrer and F. d. Monte, *J. Mater. Chem. A*, 2016, **4**, 1251-1263.
 41. K. Jurewicz, K. Babel, A. Żiółkowski and H. Wachowska, *Electrochim. Acta*, 2003, **48**, 1491-1498.
 42. J. S. Wei, H. Ding, Y. G. Wang and H. M. Xiong, *ACS Appl. Mater. Interfaces*, 2015, **7**, 5811-5819.
 43. B. Cao, B. Zhang, X. Jiang, Y. Zhang and C. Pan, *J. Power Sources*, 2011, **196**, 7868-7873.
 44. P. Chen, L. K. Wang, G. Wang, M. R. Gao, J. Ge, W. J. Yuan, Y. H. Shen, A. J. Xie and S. H. Yu, *Energy Environ. Sci.*, 2014, **7**, 4095-4103.
 45. D. Li, C. Yu, M. Wang, Y. Zhang and C. Pan, *RSC Adv.*, 2014, **4**, 55394-55399.

46. Z. Wang, L. Sun, F. Xu, X. Peng, Y. Zou, H. Chu, L. Ouyang and M. Zhu, *RSC Adv.*, 2016, **6**, 1422-1427.
47. L. Yao, G. Yang, P. Han, Z. Tang and J. Yang, *J. Power Sources*, 2016, **315**, 209-217.
48. X. Zhang, L. Ma, M. Gan, G. Fu, M. Jin, Y. Lei, P. Yang and M. Yan, *J. Power Sources*, 2017, **340**, 22-31.
49. L. Wan, J. Wang, L. Xie, Y. Sun and K. Li, *ACS Appl. Mater. Interfaces*, 2014, **6**, 15583-15596.
50. Y. Wang, X. Yang, A. G. Pandolfo, J. Ding and D. Li, *Adv. Energy Mater.*, 2016, **6**, 1600185.
51. P. M. Kharade, S. M. Mane, S. B. Kulkarni, P. B. Joshi and D. J. Salunkhe, *J. Mater. Sci.: Mater. Electron.*, 2015, **27**, 3499-3505.
52. J. Yan, Q. Wang, C. Lin, T. Wei and Z. Fan, *Adv. Energy Mater.*, 2014, **4**, 1400500.
53. P. Kleszyk, P. Ratajczak, P. Skowron, J. Jagiello, Q. Abbas, E. Frąckowiak and F. Béguin, *Carbon*, 2015, **81**, 148-157.
54. H. M. Lee, H. G. Kim, K. H. An and B. J. Kim, *Carbon Lett.*, 2014, **15**, 71-76.
55. K. Karthikeyan, S. Amaresh, S. N. Lee, X. Sun, V. Aravindan, Y. G. Lee and Y. S. Lee, *ChemSusChem*, 2014, **7**, 1435-1442.
56. L. L. Zhang, Y. Gu and X. S. Zhao, *J. Mater. Chem. A*, 2013, **1**, 9395-9408.
57. Y. Huang, E. Ma and G. Zhao, *Ind. Crop. Prod.*, 2015, **69**, 447-455.
58. M. Kılıç, E. Apaydın-Varol and A. E. Pütün, *Appl. Surf. Sci.*, 2012, **261**, 247-254.
59. D. Qu, *J. Power Sources*, 2002, **109**, 403-411.
60. O. Ioannidou and A. Zabaniotou, *Renew. Sust. Energ. Rev.*, 2007, **11**, 1966-2005.
61. A. M. Abioye and F. N. Ani, *Renew. Sust. Energ. Rev.*, 2015, **52**, 1282-1293.
62. M. A. Yahya, Z. Al-Qodah and C. W. Z. Ngah, *Renew. Sust. Energ. Rev.*, 2015, **46**, 218-235.
63. I. I. Mison, N. K. M. Zain, R. A. Aziz, B. Vidyadharan and R. Jose, *Electrochim. Acta*, 2015, **174**, 78-86.
64. M. Olivares-Marín, J. A. Fernández, M. J. Lázaro, C. Fernández-González, A. Macías-García, V. Gómez-Serrano, F. Stoeckli and T. A. Centeno, *Mater. Chem. Phys.*, 2009, **114**, 323-327.
65. X. Du, W. Zhao, Y. Wang, C. Wang, M. Chen, T. Qi, C. Hua and M. Ma,

- Bioresour. Technol.*, 2013, **149**, 31-37.
66. Q. Liang, L. Ye, Z. H. Huang, Q. Xu, Y. Bai, F. Kang and Q. H. Yang, *Nanoscale*, 2014, **6**, 13831-13837.
 67. W. H. Qu, Y. Y. Xu, A. H. Lu, X. Q. Zhang and W. C. Li, *Bioresour. Technol.*, 2015, **189**, 285-291.
 68. Y. Shen, C. Li, Y. Zhang, B. Li and Y. Fan, *Northwest University*, 2012, *CN101731367A*.
 69. J. Chu, X. Xu and Y. Zhang, *Bioresour. Technol.*, 2013, **134**, 374-376.
 70. X. M. Zang, B. Chen, C. Li, J. J. Deng, Z. Y. Wang and Y. H. Shen, *Asian J. of Chem.*, 2013, **25**, 9485-9491.
 71. K. Yang, Q. Gao, Y. Tan, W. Tian, L. Zhu and C. Yang, *Microporous Mesoporous Mater.*, 2015, **204**, 235-241.
 72. X. Wu, S. Mahalingam, A. Amir, H. Porwal, M. J. Reece, V. Naglieri, P. Colombo and M. Edirisinghe, *ACS Omega*, 2016, **1**, 202-211.
 73. S. Faraji, M. F. Yardim, D. S. Can and A. S. Sarac, *J. Appl. Polym. Sci.*, 2017, **134**, 44381.
 74. S. Peranathan, J. S. Bonso and J. P. Ferraris, *Carbon*, 2016, **106**, 20-27.
 75. F. Miao, C. Shao, X. Li, K. Wang and Y. Liu, *J. Mater. Chem. A*, 2016, **4**, 4180-4187.
 76. K. Huang, M. Li, Z. Chen, Y. Yao and X. Yang, *Electrochim. Acta*, 2015, **158**, 306-313.
 77. G. Wang and H. Uyama, *Sci. Rep.*, 2016, **6**, 21265.
 78. Y. Xin, Q. Xiong, Q. Bai, M. Miyamoto, C. Li, Y. Shen and H. Uyama, *Carbohydrate Polymers*, 2017, **157**, 429-437.
 79. S. Yoneda, W. Han, U. Hasegawa and H. Uyama, *Polymer*, 2014, **55**, 3212-3216.
 80. K. Okada, M. Nandi, J. Maruyama, T. Oka, T. Tsujimoto, K. Kondoh and H. Uyama, *Chem. Commun.*, 2011, **47**, 7422-7424.
 81. M. Nandi, K. Okada, A. Dutta, A. Bhaumik, J. Maruyama, D. Derks and H. Uyama, *Chem. Commun.*, 2012, **48**, 10283-10285.

Chapter 1

Hierarchical activated green carbons from abundant biomass waste for symmetric supercapacitors

1.1 Introduction

As described in general introduction, carbon-based electrode materials with high specific surface area and proper pore size distribution have been investigated as promising electrode candidates for supercapacitors (SCs).¹⁻³ Particularly, hierarchically porous carbon materials display even superior supercapacitor performance.⁴⁻⁶ In addition, the development and utilization of biomass resources have become a research hotspot when the costs, availability, and environmental/energy concern are totally considered.⁷⁻⁹ Therefore, the purpose of this chapter is to describe the preparation of hierarchical activated carbons from biomass and their applications on SCs.

In this chapter, the author chooses apricot shell (AS) as the biomass precursor and steam as the green activation gas to produce hierarchically activated carbons (ACs). The effects of the activation time and temperature on the specific surface area and porosity were explored systematically. The pore structure and specific surface area of ACs could be controlled by the activation conditions. The electrochemical performances of the ACs were fully evaluated on an assembled AC//AC symmetrical SC system by cyclic voltammetry (CV) and galvanostatic constant current charge/discharge (GC) measurements. The as-obtained ACs exhibited high specific surface area and well-developed hierarchical porous structure. The electrochemical results strongly suggest that the hierarchical ACs are promising for energy storage applications on SCs.

1.2 Experimental

Materials

Apricot shell collected by farmers of Baoji city (Shaanxi Province, China) was used as the starting material. Elemental analysis of AS was conducted by a CHN Corder. It showed 48.6, 5.84, and 0.13% for C, H, and N contents, respectively.

Preparation of AS-based ACs

Several hundred grams of AS were carbonized in a stainless vessel using a muffle furnace at 600 °C for 2 h to obtain chars with a weight yield of 26% for further use. The elemental analysis results of the chars were 88.3, 2.03, and 0.3% for C, H, and N contents, respectively. Subsequently, the chars (~20 g) were pyrolyzed in a rotary kiln tube furnace at an activation temperature (850, 900, or 950 °C) with heating rate of 5 °C min⁻¹ under a nitrogen atmosphere. Steam generated from deionized water was poured into the oven at a flow rate of 0.17 mL min⁻¹ and maintained for a certain time (2, 3, or 4 h) in the tube furnace after reaching the activation temperature. Then, the vaporized steam was removed from the oven and then the temperature was quickly decreased to room temperature by a cooler. In this work, the usage of the muffle furnace and the rotary kiln aimed at mass production of activated carbon from AS. Finally, the remained samples were directly ground and sieved to the size of 45 μm to obtain hierarchical activated carbons. The products were denoted as AS-x-y, standing for activated carbon prepared from AS, where x (x=850, 900, or 950 (°C)) means the activation temperature and y (y=2, 3, or 4 (h)) represents the activation time. The impurities of samples were carried out by an energy dispersive X-ray spectroscopy (EDX, Miniscope TM3000 equipped with Swift ED 3000, HITACHI). The trace elements, including O, Mg, Si, K, and Al, were contained in the prepared carbon materials. Elemental analysis showed that the carbon content exceeded 75% in all as-synthesized ACs.

Characterization

Thermogravimetric (TG) analysis was performed in the temperature range of 40~550 °C under N₂ atmosphere with a heating rate of 10 °C min⁻¹ using a Seiko EXSTAR SII TG/DTA 7200 thermal analyzer. Fourier transform infrared radiation (FTIR) analysis was conducted by a Thermo Scientific Nicolet iS5 in a wavenumber range of 4000~400 cm⁻¹. Scanning electron microscopy (SEM) and transmission electron microscope (TEM) analyses were carried out under the optimum conditions using HITACHI SU 3500 and HITACHI 7650, respectively. Nitrogen adsorption/desorption isotherms were recorded on a Quantachrome NOVA 4200e Surface Analyzer at 77 K. Prior to the tests, all the samples were outgassed at 120 °C for at least 5 h. The specific surface area was measured by Brunauer-Emmett-Teller (BET) method. The total pore volume was estimated from the adsorbed amount at a relative pressure of 0.995 and micropore volume was calculated by Horvath-Kawazoe (HK) method. Pore size distribution was determined using the non-local density functional theory (DFT) model. X-ray diffraction (XRD) analysis was obtained by using a SmartLab (Rigaku Corporation) diffractometer with Cu K α radiation from 10° to 80° under a scan rate of 0.02° min⁻¹. Raman characterization was carried out by using a NRS-3100 spectrometer (JASCO Corporation) with the laser wavelength of 532 nm. X-ray photoelectron spectroscopic (XPS) measurement was performed on an AXIS-ULTRA DLD spectrometer (Kratos Analytical) with Al K α radiation as X-ray source for excitation.

Electrochemical measurement

The electrochemical measurements were carried out in a two-electrode cell at ambient temperature on a CHI7002E electrochemical instrument (BAS Inc. ALS 7002E) using 20 wt% H₂SO₄ aqueous as electrolyte. The working electrode was fabricated as follows. The as-obtained ACs were mixed with polytetrafluoroethylene (PTFE) at a weight ratio of 90:10 in ethanol under stirring to obtain the homogenized mixture. The blended slurry was rolled into a thin film, and then it was dried at 120 °C

for more than 3 h. Before electrochemical tests, the film was firstly punched into a circular sheet (diameter of 6 mm, ~5 mg), which was sufficiently vacuum-impregnated with an electrolyte of 20 wt% H₂SO₄ solution to obtain the electrode. The AC//AC symmetric SC system was assembled in a 2E-CELL-SUS cell (Eager Corporation, Japan) with two nearly identical (weight and size) AC films using polypropylene non-woven as a separator (Fig. 1-1). CV and GC measurements were performed in the potential window from 0 to 1.0 V. The cycle performance of the as-assembled SC was evaluated by GC measurement at a current density of 5 A g⁻¹ for 6000 cycles.

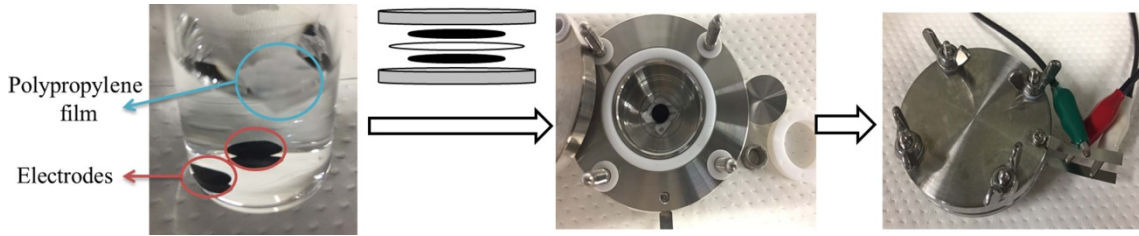


Figure 1-1. Scheme of the as-assemble AC//AC symmetric SC by a 2E-CELL-SUS cell.

In this electrode system, the specific capacitance of the total symmetrical cell (C_t , F g⁻¹) was obtained based on the GC measurements from the equation:

$$C_t = (I \times \Delta t) / (2m \times \Delta V) \quad (1-1)$$

where I (A) is the charge/discharge current, Δt (s) is the discharging time excluding the IR drop, m (g) is the mass of active sample on the single electrode, and ΔV (V) is the voltage change excluding the IR drop during the discharge process.

The energy density (E_t , Wh kg⁻¹) and power density (P_t , W kg⁻¹) of the symmetric SC system were calculated according to the following equations:

$$E_t = (C_t \times \Delta V^2) / (2 \times 3.6) \quad (1-2)$$

$$P_t = E_t / \Delta t \quad (1-3)$$

where Δt (s) and ΔV (V) are the same definitions in the previous equation.

1.3 Results and Discussion

Morphology and composition of apricot shell

The surface morphology of AS looked an undeveloped honeycomb structure, which was somewhat different with that of the edge (Fig. 1-2a and b). The main functional groups of AS were analyzed by FTIR spectrum (Fig. 1-2c). The broad peak at 3420 cm^{-1} was assigned to the stretching vibration of hydroxyl groups and the two peaks around 2900 cm^{-1} were ascribed to the symmetric and asymmetric stretching vibration of methylene groups. A peak at 1722 cm^{-1} was identified as carboxylic group, which may be regarded as evidence for the complexity of biomass materials. The $1500\text{--}1000\text{ cm}^{-1}$ region showed quite complex due to the existence of C–O, C–X (X=Cl, Br, etc) or C–C stretching vibration.¹⁰ The bond at 1215 cm^{-1} was related to ether groups formed from phenolic hydroxyl and methylol groups. The peak at 1035 cm^{-1} was ascribed to C–O stretching vibration from phenolic hydroxyl groups. These data suggest that AS is a kind of lignocellulosic biomass with various functional groups in different types of atomic linkages. Thermal stability of AS was evaluated by TG/DTA analysis under an inert atmosphere. The TG curve showed the dramatic mass loss during the pyrolysis process from around 200 to 400 °C and the DTG curve demonstrated sharp peaks at 300 and 355 °C (Fig. 1-2d). The resulting carbon residues were 27.7% and 22.8% at 400 °C and 500 °C, respectively. The mass loss occurred primarily due to the escape of H and O atoms of light volatile compounds which might be produced by the thermal decomposition of cellulose and hemicellulose before 400 °C.^{11, 12} The mass loss became slower over 400 °C, which was probably derived from the decomposition of lignin and carbon skeleton formed preliminarily.¹³ It could be seen that the yield of chars (26% at 600 °C) was higher than that of TG results at 500 °C (22.8%), which was mainly attributed to the weight of the precursor. In the preparation of AS chars, the several hundred grams of AS was used. But in the TG/DTA analysis, the sample weight was about 6 mg.

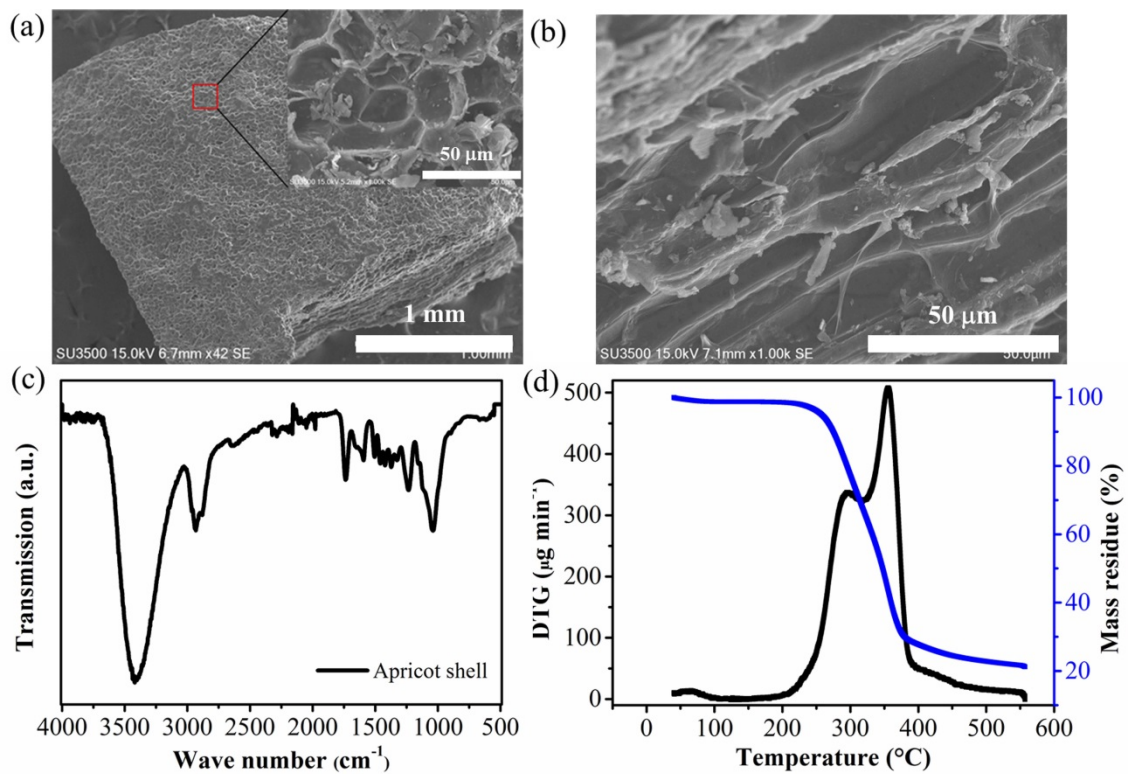


Figure 1-2. SEM images of apricot shell bulk (the inset is the surface image) (a); SEM image of the edge (b); FTIR spectrum of apricot shell (c); TG curve of apricot shell under an inert atmosphere (d).

Characterization of AS-derived activated carbons

To understand the influence of activation conditions on the development of pore structure, N_2 adsorption/desorption measurements were conducted. The obtained isotherms were shown in Fig. 1-3a. ACs prepared by lower activation temperature (AS-850-3) or shorter activation time (AS-900-2) exhibited Type I (typical of microporous carbons) isotherms, while others displayed a combination of Type I and IV (characteristic of mesoporous materials) isotherms according to the IUPAC classification, indicating that the well-developed micro/mesopore texture of the present ACs.¹⁴ The obvious hysteresis loops at 0.5-0.8 P/P_0 and rise at high relative pressure from 0.97 to 1.0 P/P_0 presented the existence of smaller slit-shaped mesopores and macropores. Therefore, AS-900-3, AS-950-3, and AS-900-4 exhibited hierarchically porous structures including abundant micropores, plentiful mesopores, and a few

macropores, meaning the significant influence of the activation conditions on the formation of the hierarchically porous structure. Fig. 1-3b showed the curves of pore size distributions calculated by DFT model. It was obvious that AC prepared by high temperature or long time possessed peaks centering at 1.5 and 1.8 nm which were defined as micropores, and several lower peaks centering at 2.3, 2.6, and 3.75 nm which belonged to mesopores.

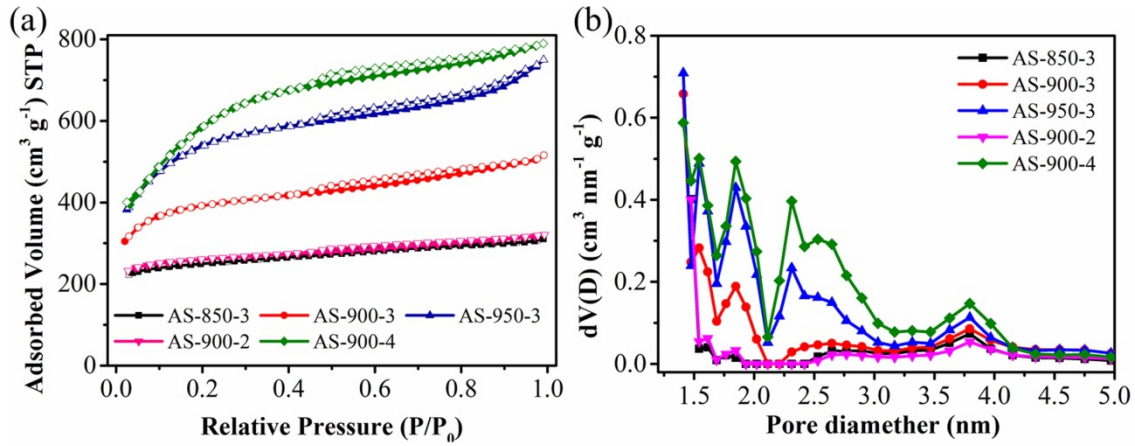


Figure 1-3. N₂ adsorption-desorption isotherms (filled: adsorption; hollow: desorption) of ACs obtained *via* different conditions (a) and pore size distribution of ACs by DFT method (b).

Table 1-1. Pore structure of the obtained AC samples and the electrochemical properties of the assembled symmetric SC.

| samples | S _{BET} ^a (m ² g ⁻¹) | V _t ^b (cm ³ g ⁻¹) | V _{mi} ^c (cm ³ g ⁻¹) | V _{me} ^d (cm ³ g ⁻¹) | V _{meso} /V _{micro} (%) | D _a ^e (nm) | C _t ^f (F g ⁻¹) |
|----------|--|---|--|--|--|-------------------------------------|---|
| AS-850-3 | 780 | 0.48 | 0.38 | 0.10 | 26 | 2.47 | 25.8 |
| AS-900-3 | 1240 | 0.80 | 0.59 | 0.21 | 36 | 2.58 | 38.3 |
| AS-950-3 | 1770 | 1.16 | 0.80 | 0.36 | 45 | 2.62 | 35.5 |
| AS-900-2 | 806 | 0.5 | 0.4 | 0.1 | 25 | 2.47 | 30.5 |
| AS-900-4 | 1910 | 1.15 | 0.80 | 0.35 | 44 | 2.42 | 37.8 |

^a S_{BET} was calculated by BET method. ^b Total pore volume (V_t) was calculated at P/P₀ = 0.99. ^c Micropore volume (V_{mi}) was calculated by HK method. ^d Mesopore volume (V_{me}) was obtained by subtracting the micropore volume from the total pore volume. ^e Average pore diameter (D_a). ^f The specific capacitance of the total symmetric SC system (C_t) was calculated from GC curves at current density of 0.05 A g⁻¹.

The BET specific surface area and the porosities parameters were summarized in Table 1-1. The surface areas of all the samples were in the range of 780–1910 m² g⁻¹. The BET surface area and total pore volume gradually increased with the rising of the activation temperature or the prolonging of the activation time.

Table 1-2. Yield and element analysis results of the samples prepared by different conditions.

| Sample | Yield (%) ^a | C (%) | H (%) | N (%) |
|----------|------------------------|-------|-------|-------|
| AS-850-3 | 61.3 | 88.7 | 0.77 | 0.18 |
| AS-900-3 | 45.9 | 85.4 | 0.91 | 0.13 |
| AS-950-3 | 25.3 | 77.3 | 1.06 | 0.12 |
| AS-900-2 | 60.8 | 81.7 | 1.35 | 0.21 |
| AS-900-4 | 28.5 | 82.7 | 0.47 | 0.13 |

^a Defined as weight of the resulting AC per that of the chars for activation.

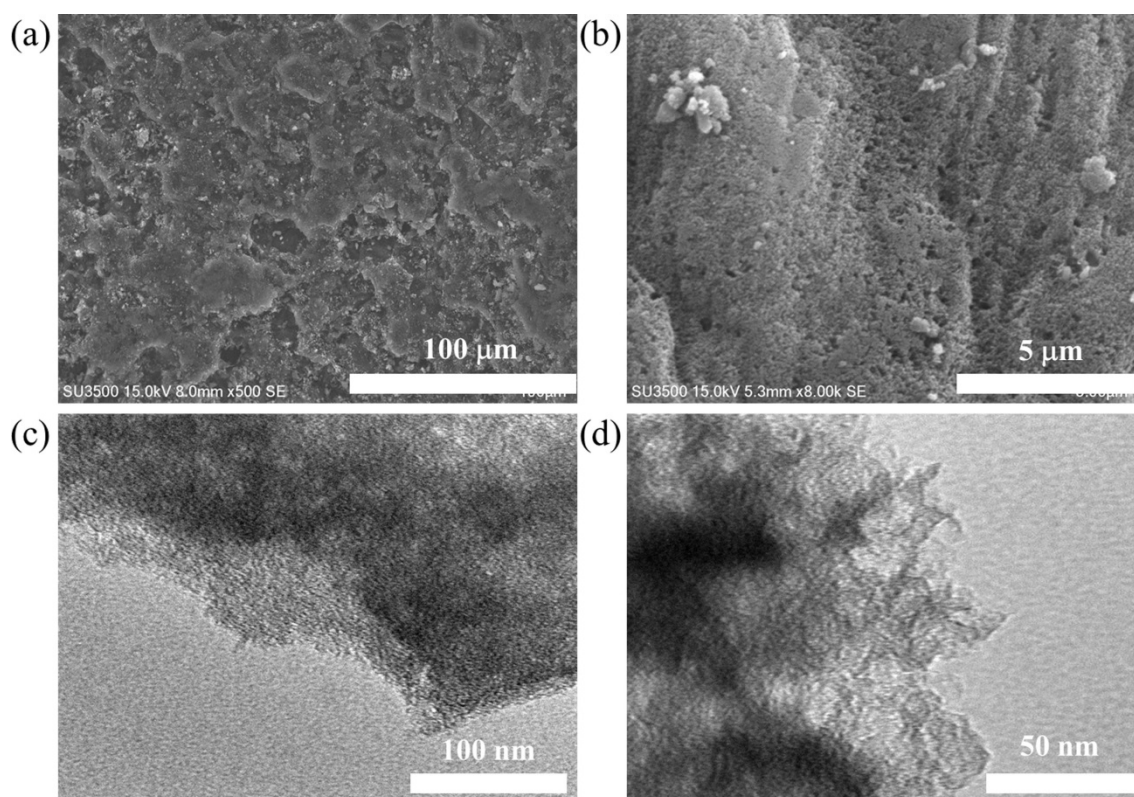


Figure 1-4. Representative SEM (a and b) and TEM (c and d) images of AS-900-3.

The yields of ACs showed the opposite trend to that of pore development (Table 1-2). Representative SEM and TEM images of AS-900-3 were shown in Fig. 1-4. It could be seen that the obtained carbon exhibited the irregular shape with rather rough surface and the high-magnification SEM revealed that the sample consisted of the porous structure. The micro-morphology and structure were also examined by TEM measurement. AS-900-3 showed the spongy and porous structure with large specific surface area.

Fig. 1-5a showed XRD patterns of the samples prepared by 900 °C under different activation times to investigate the crystalline structure. Two broad peaks including (002) diffraction at 24° and (10) diffraction at 43° represented the turbostratic structure, which also indicates that the obtained ACs were composed of graphite-like micro-crystallites that were randomly oriented and distributed throughout the ACs.⁸ With the prolonging of activation time, the (002) peak began to slightly shift towards left and the intensity became weaker, corresponding to more disordered and smaller size crystallites, which revealed the formation of the developed pore structure. By comparison of the intensity of (002) peak, the graphitization degree was found to decrease, whereas the visible peak at 43° clearly showed the higher degree of interlayer condensation, which should greatly improve the electrical conductivity.¹⁵ The presence of other characteristic peaks was attributed to other impurities which may be brought by the natural properties of apricot shell. The surface elemental compositions were captured by EDX spectroscopy. The results showed that several kinds of trace elements, including Mg, Si, K, and Al, were contained in the obtained carbons. In order to remove these inorganic impurities, the acid washing procedure will be necessary for the product carbons. Another evidence of the pore generation on the graphite-like micro-crystallites was the change of D band and G band in Raman spectroscopic analysis (Fig. 1-5b). All the samples exhibited two bands at around 1335 cm⁻¹ (D band) and 1595 cm⁻¹ (G band). The D band is associated with the disordered defects in the carbon structure, while G band is related to the ordered graphitic structure.¹⁶ It is well known that the introduction

of nanopores on graphene sheets usually leads to increase of defective and disordered structure.¹⁷ Thus, the integral intensity ratio of D band and G band (I_D/I_G) can be used as a measure of the degree of graphitization, and the smaller the I_D/I_G ratio means the higher the degree of graphitization. The I_D/I_G ratios of AS-900-2, AS-900-3, and AS-900-4 were determined to be 1.04, 1.08, and 1.15, respectively. With prolonging the activation time, the I_D/I_G ratio gradually increased, suggesting the more defective and disordered structure with lower graphitization.¹⁸ AS-900-3 displayed the higher graphitization degree than AS-900-4, indicating a better electrical conductivity which will be beneficial for the further electrochemical performance. The above data of N_2 adsorption, SEM and TEM images, XRD pattern, and Raman spectra suggest that the present ACs prepared from apricot shell were porous carbon materials with turbostratic structures.

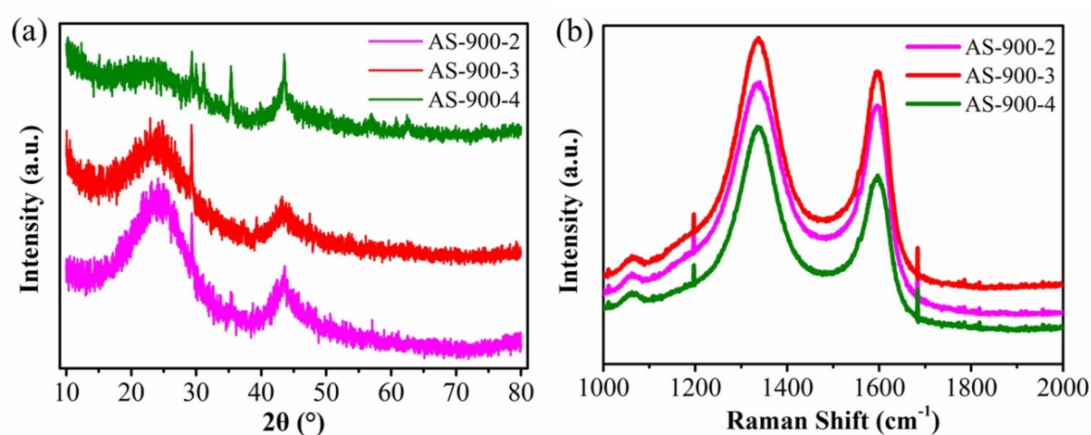


Figure 1-5. XRD patterns (a) and Raman spectra (b) of AS-900-2, AS-900-3, and AS-900-4.

The chemical compositions of AS-900-4 and the chemical status of carbon and oxygen were determined by XPS spectra (Fig. 1-6). It exhibited a predominant C 1s peak at 284.6 eV and an obvious O 1s peak at 531.6 eV. The contents of C and O were 92.1% and 7.9%, respectively. To obtain the detailed information, the high-resolution XPS spectrum of C 1s was collected, which was deconvoluted into four sub-peaks centered at 284.6 eV, 285.6 eV, 286.5 eV, and 287.6 eV (Fig. 1-6a). These peaks

correspond to sp^2 -hybridized graphite-like carbon (sp^2 C), sp^3 -hybridized diamond-like carbon (sp^3 C), C-O/C-N, and C=O/C=N, respectively.¹⁹ The O 1s peaks at 531.1 eV, 532.4 eV, and 533.8 eV were assigned to C=O group, C-O (oxygen in esters or in hydroxyls), and C-O (oxygen in carboxyl groups), respectively. These oxygen-containing functionalities would promote the wettability and acid/base character of ACs for generation of additional pseudo-capacitance to enhance the overall capacitance.⁸

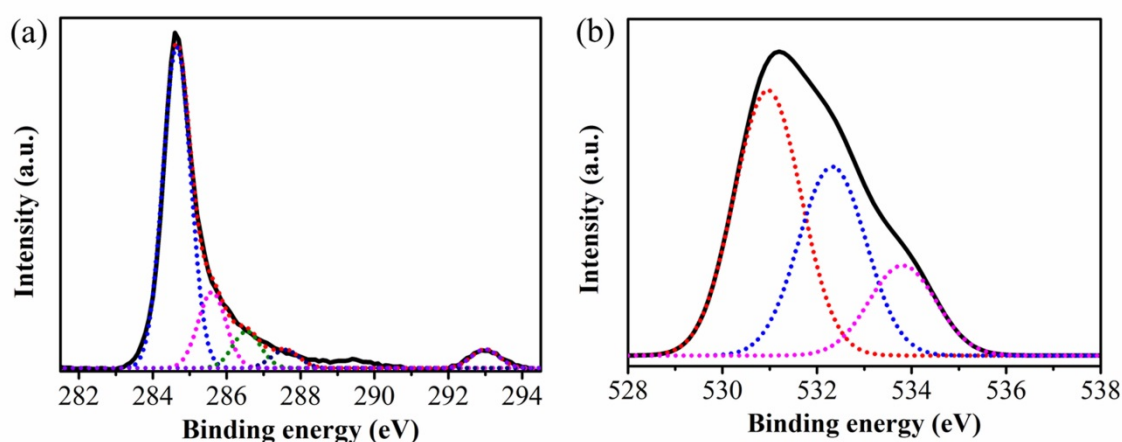


Figure 1-6. High-resolution XPS spectra of C 1s peak (a) and O 1s peak (b) of AS-900-4.

Electrochemical performance of AS-derived activated carbons

The electrochemical properties of the obtained AS-derived ACs as electrode materials for SC were initially evaluated in an AC//AC symmetric SC system with 20 wt% H_2SO_4 as an aqueous electrolyte. CV curves at scan rate of 10 mV s^{-1} were shown in Fig. 1-7a. All the samples exhibited nearly rectangular shapes, indicating a typical SC behavior with excellent rate capability.²⁰ Moreover, the CV curve of AS-900-3 presented the largest integral area in this potential region, suggesting the highest capacitance among these samples. The CV curves exhibited an approximately rectangular shape under various potential windows, presenting a good stability in the 20 wt% H_2SO_4 electrolyte. The rate capability is an important factor for use of SC in energy storage applications. CV tests at different scan rates were also investigated to

evaluate the electrochemical performance of electrodes (Fig. 1-7b). For the CV curves of AS-900-3, an approximately rectangular shape was still maintained even at a scan rate of 100 mV s^{-1} , implying the remarkable electric performance under the high rate operation.

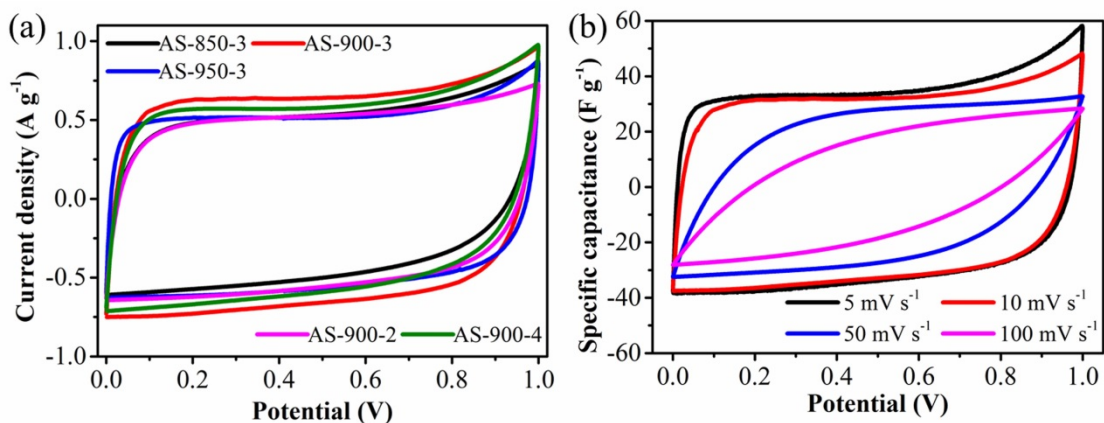


Figure 1-7. CV curves of AC//AC symmetric SC at scan rate of 10 mV s^{-1} (a) and CV curves of AS-900-3-based SC at different scan rates from 5 to 100 mV s^{-1} (b).

GC curves of all the samples at constant current density of 0.5 A g^{-1} exhibited typical triangle shapes and low resistance related to voltage drops (Fig. 1-8a), revealing that the AS-derived ACs had excellent coulombic efficiency together with good double-layer capacitive performance.²¹ The specific capacitances at various current densities were calculated and plotted in Fig. 1-8b. The specific capacitance values of the assembled SC system (C_t) are 24.5 F g^{-1} for AS-850-3, 36.8 F g^{-1} for AS-900-3, 32 F g^{-1} for AS-950-3, 29.5 F g^{-1} for AS-900-2, and 35.3 F g^{-1} for AS-900-4 from the discharge curves at a current density of 0.1 A g^{-1} . It was obvious that AS-900-3 possessed the highest specific capacitance at both low and high current densities, which was as high as 38.3 F g^{-1} at 0.05 A g^{-1} and 73% of this value remained when the current density increased to 100-fold. In comparison with AS-900-4 and AS-950-3, AS-900-3 possessed lower surface area but higher specific capacitance, which could be attributed to the more suitable porous structure of AS-900-3. As shown in Table 1-1, AS-900-4 and AS-950-3 showed higher $V_{\text{meso}}/V_{\text{micro}}$ value but the real and effective pores for the

electrolyte ions were less than AS-900-3, resulting that AS-900-3 displayed a higher specific capacitance. Based on the above discussion, it could be speculated that AS-900-3 possessing a relatively high surface area displayed a more proper porous structure for the as-assembled SC than AS-900-4 and AS-950-3.

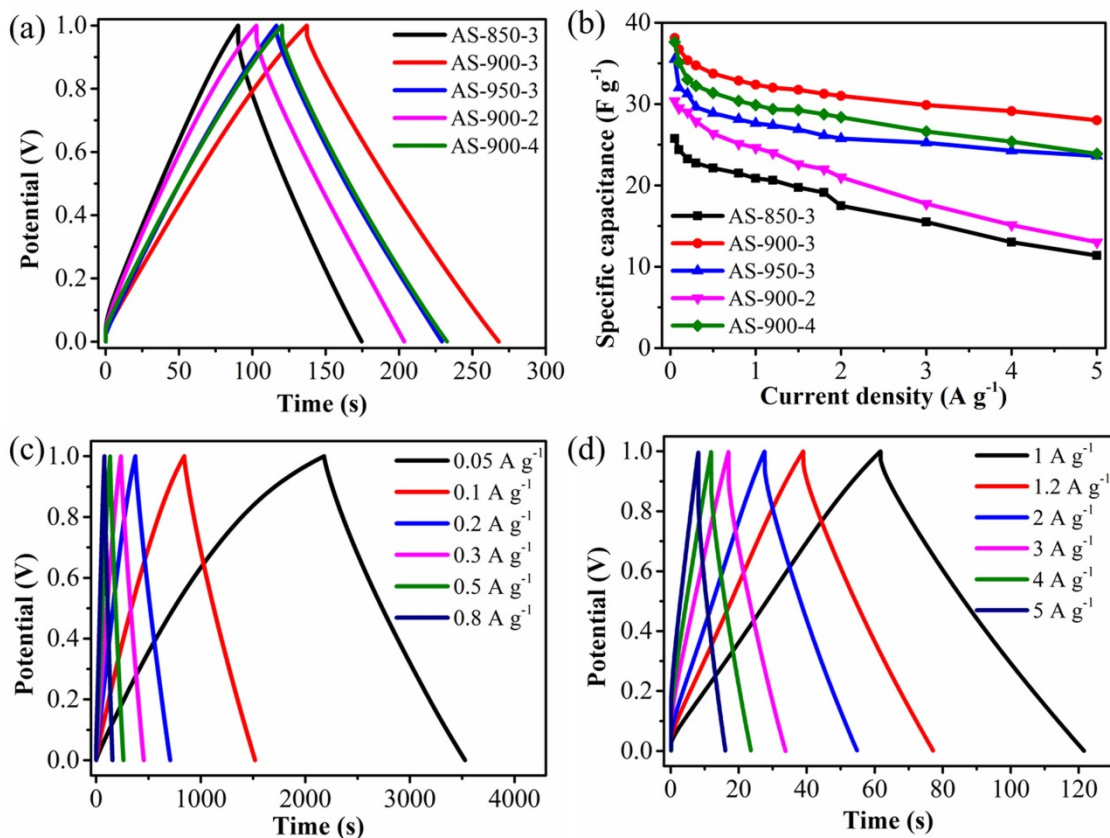


Figure 1-8. GC curves of AC//AC symmetric SC at constant current density of 0.5 A g⁻¹ (a) and specific capacitances of the SC system at different current densities (b); GC curves of AS-900-3-based SC at different current densities from 0.05 to 0.8 A g⁻¹ (c) and from 1 to 5 A g⁻¹ (d).

The capacitances of AS-900-3 slightly decreased with increasing the current densities, implying that the present carbons allowed rapid ion diffusion. These data indicate that the present hierarchically porous activated carbons derived from apricot shell displayed the moderate electrochemical performance, comparable to that of many reported biomass-based carbons (Table 1-3). For the GC curves of AS-900-3, the triangular-like shapes remained from the constant current density of 0.05 A g⁻¹ even to 5

A g^{-1} (Fig. 1-8c and d), demonstrating the ideal charge and discharge characteristics for SC. The excellent high-rate ion transport property would be ascribed to the well-developed micro-mesoporous structure.²² It was found that the presence of a relatively small IR drop at the beginning of the discharge process even in a high current density suggested a low equivalent series resistance in the symmetric SC and good electrochemical stability. All the above results clearly demonstrate the good electrochemical performance of AS-900-3 for SC electrodes with high capability, suggesting that the electrolyte ions could efficiently, rapidly, and fully penetrate into the interface of the porous activated carbon electrodes even at the high current density. The superior characters of the present electrodes are probably attributed to their high specific surface area and hierarchically interconnected porous structures.

Table 1-3. Biomass derived carbon materials as electrodes in a two-electrode system.

| Precursors | Activators | S_{BET} ($\text{m}^2 \text{g}^{-1}$) | Electrolyte | C_s^a (F g^{-1}) |
|---|--------------------------------------|---|---------------------------------------|-------------------------------|
| Ramie ²³ | ZnCl ₂ | 1616 | 6 M KOH | 287 |
| Fallen leaves ¹⁴ | KOH & K ₂ CO ₃ | 1078 | 6 M KOH | 242 |
| Corn husk ⁸ | KOH | 867 | 6 M KOH | 260 |
| BP stem Bark ¹⁹ | KOH | 1212 | 6 M KOH | 258 |
| Sunflower shell ²⁴ | KOH | 2509 | 30 wt% KOH | 311 |
| Pomelo peel ²⁵ | KOH | 2057 | 1 M NaNO ₃ | 174 |
| Coconut-shell ²⁶ | Steam | 1532 | 6 M KOH | 192 |
| Corn cob residue ²⁷ | Steam | 1210 | 6 M KOH | 120 |
| <i>Amygdalus pedunculata</i> shell (APS) | K ₂ CO ₃ | 2030 | 20 wt% H ₂ SO ₄ | 210 |
| Apricot shell (This work) | Steam | 1240 | 20 wt% H ₂ SO ₄ | 153 |

^a Specific capacitance of the single electrode.

Based on the results of specific capacitances, the energy density and power density of the SC were calculated. Fig. 1-9a showed Ragone plots related to the correlation between power output and energy density of the obtained electrodes. There was a decreasing trend in the power density with the increase of energy density for all the electrodes, which was attributed to the complex resistance and tortuous diffusion pathway within the porous structures.^{14,28} The energy density also could be impacted by

the precursor of carbon materials and preparation methods.^{22, 29} Cycling stability is considered as another crucial factor in practical applications. Therefore, the cycling life of AS-900-3-based symmetric SC was conducted by GC measurement at current density of 5 A g⁻¹. As shown in Fig. 1-9b, AS-900-3 exhibited high capacitance retention (99% of its initial capacitance) after 6000 cycles, implying excellent electrochemical cycling stability.

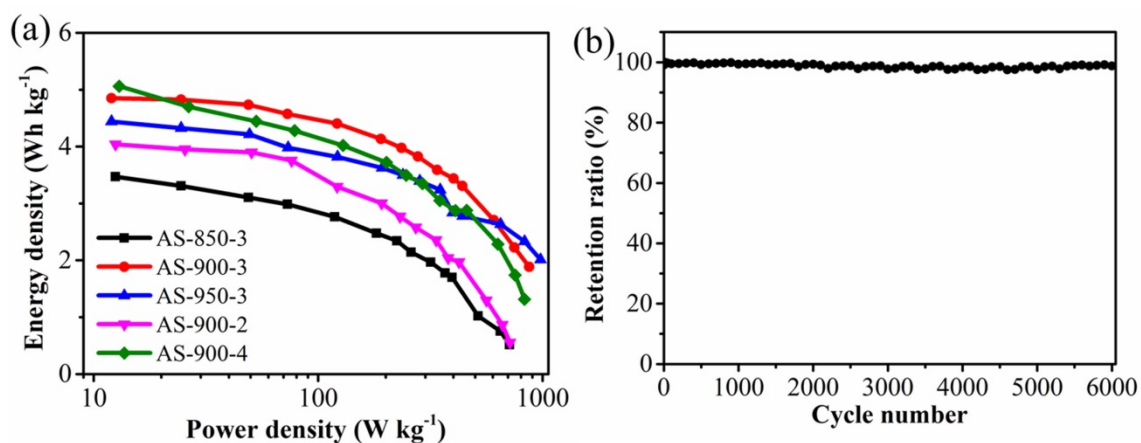


Figure 1-9. Ragone plots referring to energy and power density of AC//AC symmetric SC (a) and cycling performance of AS-900-3-based SC at current density of 5 A g⁻¹ (b).

1.4 Conclusion

Hierarchically porous ACs have been successfully produced from apricot shell *via* a carbonization process, followed by a green and low-cost steam activation. The as-synthesized ACs possessed the turbostratic carbon structure with high specific area and moderate porous distribution. The fabricated AC//AC symmetric SC displayed the superior electrochemical performance and AS-900-3-based electrode showed large specific capacitance, high capacitance retention, and long cycle life.

This chapter demonstrates an effective utilization route of AS, a renewable and sustainable biomass waste for SC electrodes. Hierarchical ACs have been obtained by systematical screening of carbonization and activation of AS. As described above, the present study reveals a feasible approach for the large-scale and low-cost production of high-performance electrode materials for SC from AS.

1.5 References

1. Q. Wang, J. Yan and Z. Fan, *Energy Environ. Sci.*, 2016, **9**, 729-762.
2. F. Beguin, V. Presser, A. Balducci and E. Frackowiak, *Adv. Mater.*, 2014, **26**, 2219-2251.
3. L. L. Zhang, Y. Gu and X. S. Zhao, *J. Mater. Chem. A*, 2013, **1**, 9395-9408.
4. J. S. Wei, H. Ding, Y. G. Wang and H. M. Xiong, *ACS Appl. Mater. Interfaces*, 2015, **7**, 5811-5819.
5. C. Z. Yuan, B. Gao, L. F. Shen, S. D. Yang, L. Hao, X. J. Lu, F. Zhang, L. J. Zhang and X. G. Zhang, *Nanoscale*, 2011, **3**, 529-545.
6. Y. Liu, Z. Shi, Y. Gao, W. An, Z. Cao and J. Liu, *ACS Appl. Mater. Interfaces*, 2016, **8**, 28283–28290.
7. L. Zhang, Z. Liu, G. Cui and L. Chen, *Prog. Polym. Sci.*, 2015, **43**, 136-164.
8. S. Song, F. Ma, G. Wu, D. Ma, W. Geng and J. Wan, *J. Mater. Chem. A*, 2015, **3**, 18154-18162.
9. N. Sudhan, K. Subramani, M. Karnan, N. Ilayaraja and M. Sathish, *Energy & Fuels*, 2017, **31**, 977-985.
10. Y. Huang, E. Ma and G. Zhao, *Ind. Crop. Prod.*, 2015, **69**, 447-455.
11. W. Tongpoothorn, M. Sriuttha, P. Homchan, S. Chanthai and C. Ruangviriyachai, *Chem. Eng. Res. Des.*, 2011, **89**, 335-340.
12. C. H. Huang and R. A. Doong, *Microporous Mesoporous Mater.*, 2012, **147**, 47-52.
13. B. Cagnon, X. Py, A. Guillot, F. Stoeckli and G. Chambat, *Bioresour. Technol.*, 2009, **100**, 292-298.
14. Y. T. Li, Y. T. Pi, L. M. Lu, S. H. Xu and T. Z. Ren, *J. Power Sources*, 2015, **299**, 519-528.
15. G. Xu, J. Han, B. Ding, P. Nie, J. Pan, H. Dou, H. Li and X. Zhang, *Green Chem.*, 2015, **17**, 1668-1674.
16. Q. Xie, R. Bao, A. Zheng, Y. Zhang, S. Wu, C. Xie and P. Zhao, *ACS Sustainable Chem. Eng.*, 2016, **4**, 1422-1430.

17. G. Ma, Q. Yang, K. Sun, H. Peng, F. Ran, X. Zhao and Z. Lei, *Bioresour. Technol.*, 2015, **197**, 137-142.
18. H. Li, D. Yuan, C. Tang, S. Wang, J. Sun, Z. Li, T. Tang, F. Wang, H. Gong and C. He, *Carbon*, 2016, **100**, 151-157.
19. T. Wei, X. Wei, Y. Gao and H. Li, *Electrochim. Acta*, 2015, **169**, 186-194.
20. J. Yan, Q. Wang, C. Lin, T. Wei and Z. Fan, *Adv. Energy Mater.*, 2014, **4**, 1400500.
21. B. Xu, Y. Chen, G. Wei, G. Cao, H. Zhang and Y. Yang, *Mater. Chem. Phys.*, 2010, **124**, 504-509.
22. X. Gao, W. Xing, J. Zhou, G. Wang, S. Zhuo, Z. Liu, Q. Xue and Z. Yan, *Electrochim. Acta*, 2014, **133**, 459-466.
23. X. Du, W. Zhao, Y. Wang, C. Wang, M. Chen, T. Qi, C. Hua and M. Ma, *Bioresour. Technol.*, 2013, **149**, 31-37.
24. X. Li, W. Xing, S. Zhuo, J. Zhou, F. Li, S. Z. Qiao and G. Q. Lu, *Bioresour. Technol.*, 2011, **102**, 1118-1123.
25. C. Peng, J. Lang, S. Xu and X. Wang, *RSC Adv.*, 2014, **4**, 54662-54667.
26. J. Mi, X. R. Wang, R. J. Fan, W. H. Qu and W. C. Li, *Energy & Fuels*, 2012, **26**, 5321-5329.
27. W. H. Qu, Y. Y. Xu, A. H. Lu, X. Q. Zhang and W. C. Li, *Bioresour. Technol.*, 2015, **189**, 285-291.
28. K. Karthikeyan, S. Amaresh, S. N. Lee, X. Sun, V. Aravindan, Y. G. Lee and Y. S. Lee, *ChemSusChem*, 2014, **7**, 1435-1442.
29. A. Bello, F. Barzegar, D. Momodu, J. Dangbegnon, F. Taghizadeh and N. Manyala, *Electrochim. Acta*, 2015, **151**, 386-392.

Chapter 2

Fabrication of N-doped and shape-controlled porous monolithic carbons from polyacrylonitrile for supercapacitors

2.1 Introduction

In recent years, the surface heteroatoms of carbon materials have been discovered to be one factor to influence the electrochemical performance besides the specific surface area and porosity distribution. As described in general introduction, N-doping is proved to be positive in enhancing the capacity by enhancing the electronic conductivity and surface wettability of electrode materials.¹⁻³ The approach of directly pyrolysis for N-containing polymer precursor is likely to be effective to reserve the nitrogen content after the high temperature treatment.⁴⁻⁶

In this chapter, the fabrication route of N-doped porous monolithic carbons (PMC) from polyacrylonitrile (PAN) is described. The template-free thermally induced phase separation (TIPS) approach followed by a pyrolysis process was employed. Two typical pyrolysis methods including carbon dioxide and potassium hydroxide activation were discussed and compared to obtain PMC with desired properties. The specific surface areas and porosity parameters were systematically investigated and the electrochemical performances were fully evaluated on both three- and two-electrode systems.

2.2 Experimental

Fabrication of PAN Monolith

Polyacrylonitrile copolymer (PAN) was obtained from Mitsubishi Rayon Co. Ltd.. A 3D porous monolith (PM) was fabricated *via* a template-free TIPS approach. In

this process, PAN (0.42 g) was firstly dissolved in N, N-dimethylformamide (DMF) /deionized water (DMF/H₂O, 85/15 wt %, 6 mL), and then stirred and heated at 85 °C until PAN was completely dissolved. Subsequently, the solution was cooled at 25 °C for the phase separation. The formed gel was immersed in methanol under mild shaking for removing DMF. Finally, 3D PM was obtained by drying under a reduced vacuum for one day. Meanwhile, monoliths with various shapes could be formed through the vessels used for phase separation process.

Preparation of porous monolithic carbons

At first, PM was subjected to oxidative stabilization by heating at 230 °C for 6 h under the existence of air. After naturally cooling to room temperature, the stabilized PM was calcined at 600 °C for 1 h under the argon atmosphere to obtain the pre-carbonized SPM (PSPM). Subsequently, KOH activation of PSPM was performed as follows: a given mass of PSPM was blended with KOH particles (PSPM/KOH mass ratio: 1/1), and the mixture was heated at 200 °C, 500 °C, and finally at 800 °C for 1 h in each step in a furnace under the protection of N₂ flow. After cooling down to room temperature, the sample was washed sequentially with 1 M HCl and then deionized water until the pH became neutral. Finally, the sample was dried at 105 °C for 1 day, which was denoted as PMC. For comparison, SPM was carbonized and activated in a furnace under Ar/CO₂ (75/25 wt %) atmosphere at 950 °C for 1 h. After cooling down to room temperature, the final product was taken out for use and denoted as CD-PMC.

Characterization

The detailed techniques and instruments for SEM, TG analysis, FTIR, porosity property, EDX, element analysis, XRD, and XPS measurements were described in chapter 1.

Electrochemical measurements

The electrochemical performance was evaluated in both the three- and two-electrode configurations by cyclic voltammetry (CV), galvanostatic

charge/discharge (GC), and electrochemical impedance spectroscopy (EIS) measurements.

At first, a three-electrode system was applied with 1M H₂SO₄ as the aqueous electrolyte, platinum wire as the counter electrode, Ag/AgCl as the reference electrode, and glassy carbon (4-mm diameter) as the working electrode. The working electrode was prepared as follows: 20.0 mg active samples (powder size < 45 μm) were added into 1 mL Nafion solution (0.8 wt%, diluted by isopropanol from 5% Nafion®) and sonicated for 30 min to form a well-dispersed ink, 3.5 μL of which was then dropped into the surface of the glassy carbon electrode. CV measurements were tested in a potential range of 0 to 0.8 V vs Ag/AgCl by varying scan rate from 1 to 500 mV s⁻¹. GC measurements were carried out under current density at 0.2-100 A g⁻¹ with a potential window of 0-0.8 V. The cycle performance was evaluated by the GC measurement at a constant current density of 20 A g⁻¹ for 5000 cycles. The specific capacitance (*C*, F g⁻¹) obtained from CV was calculated by the following equation:

$$C = (q_a + q_c)/(2m\Delta V) \quad (2-1)$$

where *q_a* and *q_c* are the integrated anodic and cathodic voltammetric charges, respectively; *m* and Δ*V* refer to the mass of electrode material and the potential window, respectively.

The specific capacitances (*C*, F g⁻¹) obtained from the discharge process of the GC curves were calculated by the equation:

$$C = (I \times \Delta t)/(m \times \Delta V) \quad (2-2)$$

where *I* is the current, Δ*t* is the discharging time, and Δ*V* is voltage change excluding the IR drop during the discharge process.

EIS measurement was carried out in the frequency range from 10⁻² Hz to 10⁴ Hz at 0 V with voltage amplitude of 10 mV in 1 M H₂SO₄ electrolyte. The PMC-based working electrodes were prepared as follows. A homogenized slurry consisting of 85 wt% PMC (powder size < 45 μm), 10 wt% acetylene black, and 5 wt% polytetrafluoroethylene (PTFE) binder was rolled into a thin film. Then, the film was

dried at 120 °C for one day and punched into a circular sheet (6 mm diameter). The obtained PMC-based sheet was pressed on the surface of SUS mesh as the working electrode. A platinum wire and an Ag/AgCl electrode were used as the counter electrode and the reference electrode, respectively.

The practical electrochemical performance was fully evaluated in a two-electrode system by using 1 M H₂SO₄ aqueous solution as electrolyte. The weight of each electrode was around 2 mg. For comparison, commercial activated carbon (YP-50F, Kuraray Chemical Co.) was also tested under the same conditions. The detailed assemble scheme and the performance evaluation for the symmetrical system were similar to the descriptions appeared in chapter 1.

2.3 Results and Discussion

Fabrication of monolith and its properties

Fig. 2-1a showed the fabrication process of PM *via* the TIPS approach. The SEM images revealed that the raw PAN particle displayed a spherical shape but the fabricated PM exhibited a 3D porous structure (Fig. 2-1b and c), indicating that this TIPS approach promoted the successful formation of highly cross-linked meso/macro-porous network. The various shapes of PM were designed during the phase separation process and the 3D structure of these PM still remained unchanged (Fig. 2-2), revealing the feasible of the formation of shape-controlled product carbons. Thermal degradation behaviors of the PAN powder and PM were studied by the TG analysis (Fig. 2-1d). The dramatic weight loss occurred from 320 to 460 °C, suggesting that the pyrolysis took place and volatile gases came out.⁷ The resulting weight residues were about 49% at 500 °C for the prepared PM. Obviously, PM showed a higher total weight residue than that of the raw PAN powder, which may be due to the formation of internal 3D network and beneficial to get higher product yield after the further activation process.

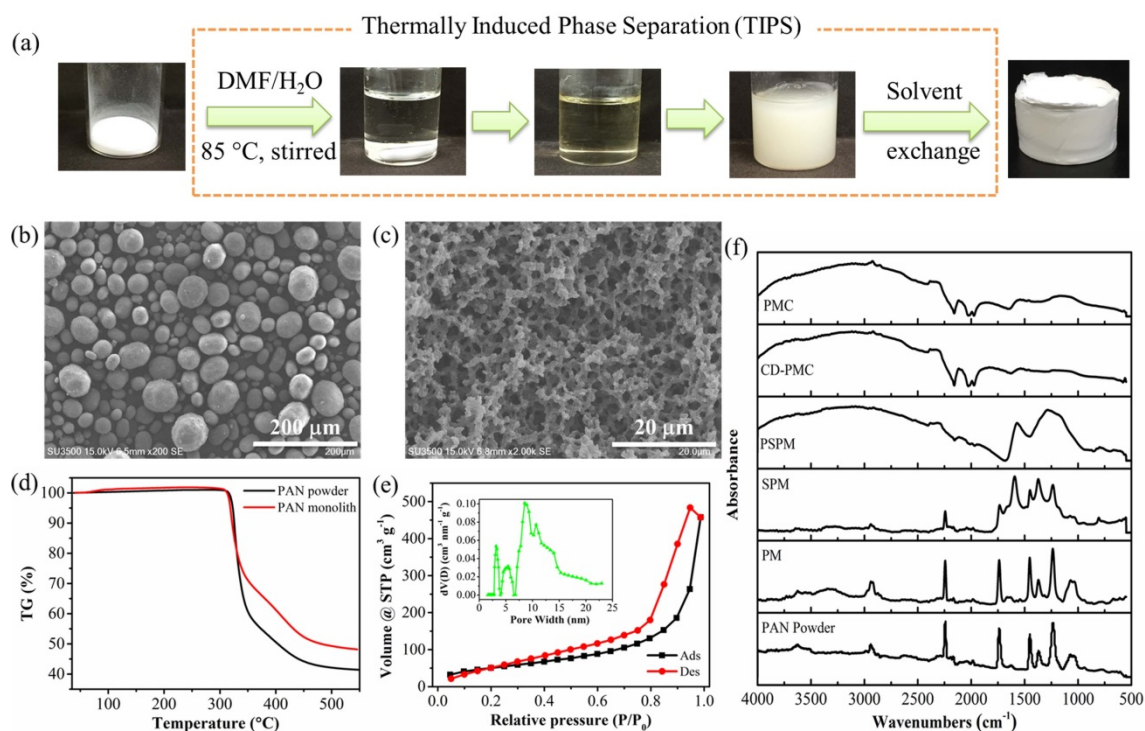


Figure 2-1. The fabrication process of 3D PM *via* a template-free TIPS technique (a), SEM images of the raw PAN powder (b) and the obtained PM (c), TG curves of the raw PAN powder and the fabricated PM (d), Nitrogen adsorption/desorption isotherms with the inset of pore size distribution calculated by DFT model of PM (e), FTIR spectra of all related products from raw PAN powder to PMC (f).

The nitrogen adsorption/desorption isotherms of PM followed the typical type IV isotherm with a large hysteresis loop at high relative pressure, which means the presence of more or less disordered cylindrical or wedge-like pores (Fig. 2-1e). The obtained PM showed the BET surface area of $188 \text{ m}^2 \text{ g}^{-1}$ with the pore volume of $0.71 \text{ cm}^3 \text{ g}^{-1}$ and average pore size of 15 nm. The pore size distribution calculated by the non-local density functional theory (DFT) model exhibited a hierarchically porous structure including a few micropores, abundant mesopores and macropores (Fig. 2-1e, inset). The functional groups were analyzed by FTIR spectra (Fig. 2-1f). There was no clear difference between the raw PAN powder and obtained PM. Furthermore, the surface elemental compositions of them were captured by EDX measurement (Table 2-1). The C, N, and O contents of PM were 67, 27, and 5.9 wt%, respectively. The

fabricated PM possessed the advantages of 3D hierarchical porous structure and enriched heteroatoms contents, endowing them with the great potential to further prepare porous carbons with large surface area, uniform pore distribution, and high nitrogen content.

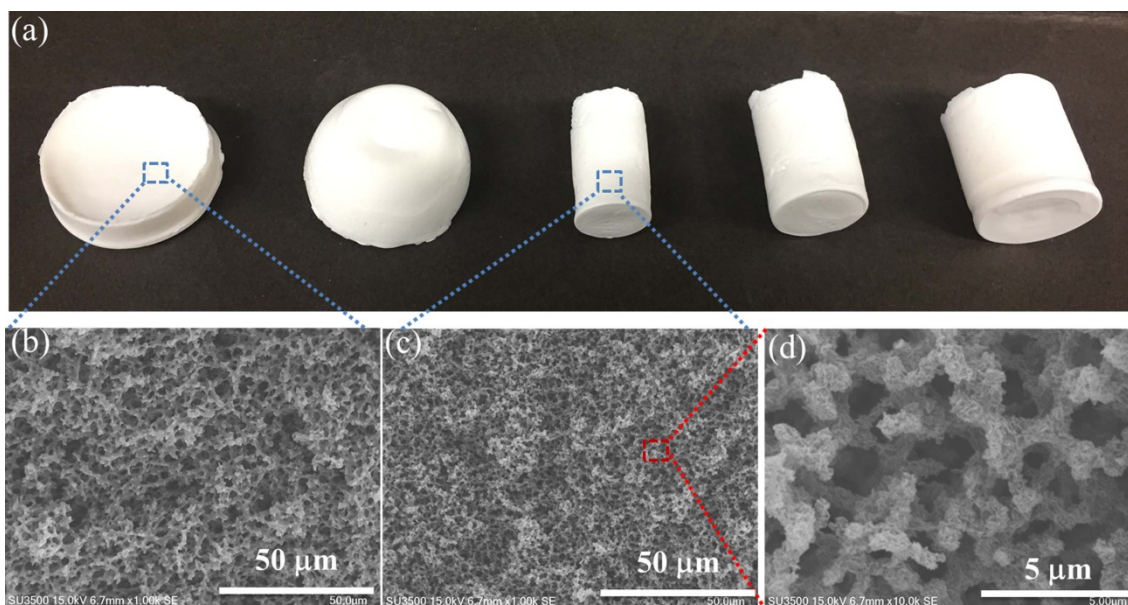


Figure 2-2. PM fabricated by the TIPS approach with various shapes (a), SEM images of the obtained PM (b-d).

Preparation and characterization of PAN-based monolithic carbon

Two thermal treatment steps including stabilization (or pre-oxidation) and carbonization are necessary for the production of PAN-based carbons due to the property of pseudo-graphite microcrystal.⁷ Stabilization process forms an infusible stable ladder structure which might be able to withstand high temperature during pyrolysis process; and the carbonization promotes to keep out non-carbon atoms and yield a turbostratic structure.⁸ Thus, PM was firstly stabilized at 230 °C for 6 h under air to get the SPM. The primary reactions during this process, including oxidation, dehydrogenation, and cyclization, were speculated by FTIR spectra (Fig. 2-1f). The dramatic decrease in 2240 cm^{-1} ($\text{C}\equiv\text{N}$ band) and obvious increase in 1587 cm^{-1} ($\text{C}=\text{N}$ band) compared with that of PM, which can be interpreted by the 6-membered

cyclization involving the formation of C=N.^{7,9} The appearance of a small band at 805 cm^{-1} corresponded to C=C-H stretching vibration revealed the dehydrogenation and subsequent isomerization of PM in this stabilization process.¹⁰

After the stabilization, two methods were chosen to prepare porous monolithic carbons, one was that SPM was directly activated under the existence of carbon dioxide to obtain CD-PMC; another was that SPM was first carbonized in the argon gas and then activated with an equal weight of KOH to get PMC. The micromorphology and microstructure of all samples were studied by SEM images (Fig. 2-3). No significant differences can be observed in the external shape of the four samples and the interconnected 3D porous structures still remained even after activation process.

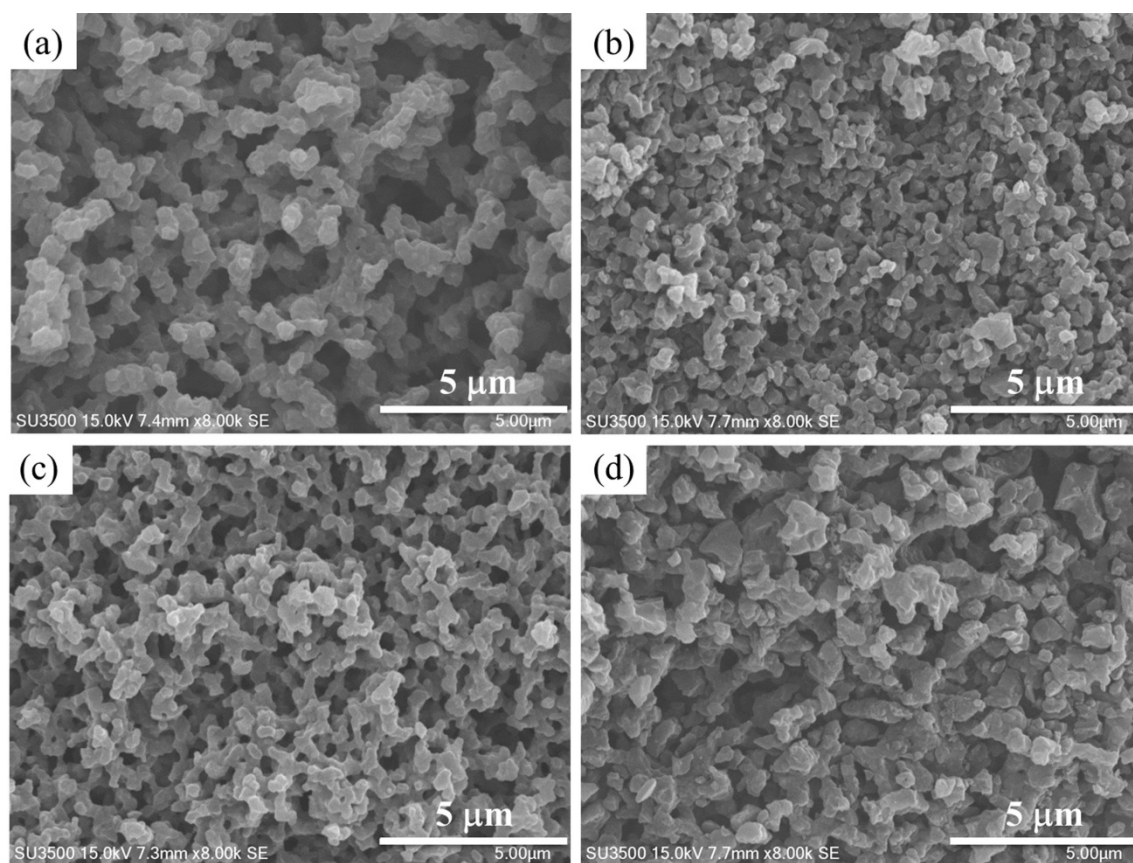


Figure 2-3. SEM images of SPM (a), CD-PMC (b), PSPM (c), and PMC (d) under a same magnification.

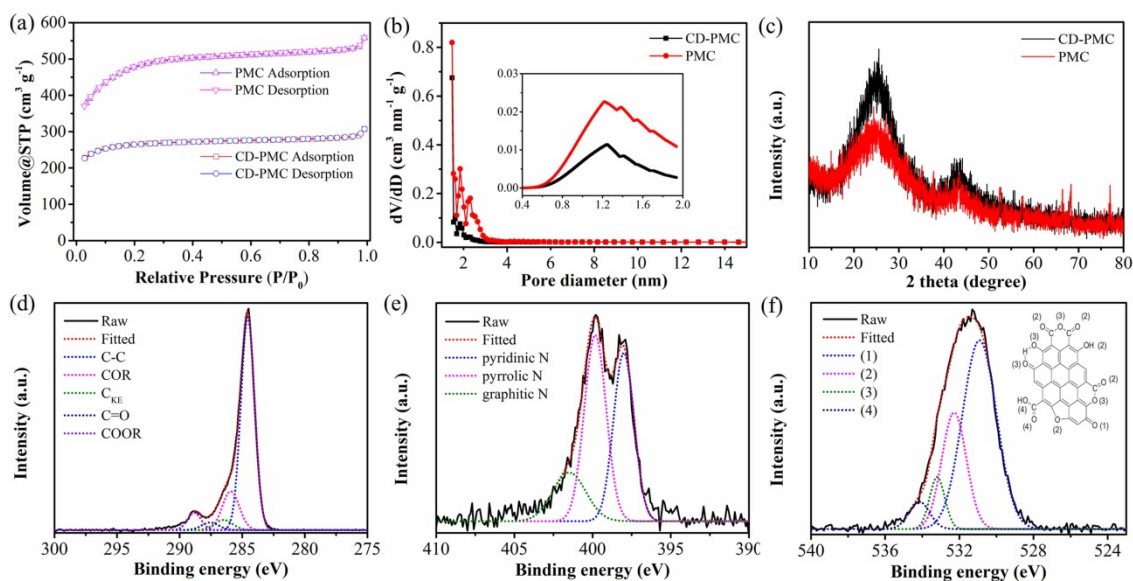


Figure 2-4. N₂ adsorption/desorption isotherms (a) and pore size distributions calculated by DFT method with an inset of that by HK method (b) of CD-PMC and PMC, XRD patterns of CD-PMC and PMC (c), High-resolution XPS spectra and fitted data of C 1s peak (d), N 1s peak (e), and O 1s peak (f) for PMC.

The nitrogen adsorption/desorption isotherms and pore size distributions were illustrated to analyze the pore structure of PMC and CD-PMC. As shown in Fig. 2-4a, they both exhibited a type-I isotherm, while PMC possessed higher adsorbed volume. The pore size distribution was mostly smaller than 4 nm from DFT method and microporous size from the HK model was mainly distributed between 0.8 to 2 nm with a peak around 1.2 nm (Fig. 2-4b). The specific surface areas of PMC and CD-PMC measured by BET method were 1600 and 700 m² g⁻¹, which were much higher than that of PM. A detailed description of the specific surface area, pore volume, average pore size, and chemical composition of all samples were presented in Table 2-1. It can be seen that approximately 27 wt% of nitrogen was detected for PM and SPM from EDX spectrum, while 3.2% and 5.6% were obtained for CD-PMC and PMC from a CHN coder. The nitrogen content decreased and carbon content increased after carbonization and activation process. Fig. 2-4c showed XRD patterns of CD-PMC and PMC. There were two characteristic peaks observed at around 24° and 43°, corresponding to the (002) and (10) diffractions, respectively. The XRD pattern of PMC showed weaker

peak intensities than those of CD-PMC, corresponding to more disordered and smaller crystallites, which suggested the formation of the developed pore structure and relatively low graphitization degree.

Table 2-1. BET surface area, total pore volume, average pore diameter, and chemical compositions of all samples.

| Sample | From N ₂ adsorption at 77 K | | | From EDX (wt%) or a CHN Corder (%) | | | |
|---------------|--|---|---------------------------------------|------------------------------------|------------|------------|----------|
| | S _{BET} ^a (m ² g ⁻¹) | V _{total} ^b (cm ³ g ⁻¹) | D _{ave} ^c (nm) | C (wt%) | N (wt%) | O (wt%) | H (%) |
| Raw | - | - | - | 67 | 28 | 5.2 | - |
| PAN | - | - | - | - | - | - | - |
| PM | 188 | 0.710 | 15.1 | 67 | 27 | 5.9 | - |
| SPM | - | - | - | 66 | 27 | 6.9 | - |
| PSPM | 8.95 | 0.017 | 7.57 | 71 (71%) | 26 (19%) | 3.5 | 2.1 |
| CD-PMC | 722 | 0.493 | 2.73 | 86 (72%) | 7.8 (3.2%) | 5.3 | 1.7 |
| PMC | 1600 | 0.862 | 2.16 | 83 (80%) | 10 (5.6%) | 6.0 | 0.5 |

^a S_{BET} calculated by BET method. ^b Total pore volume (V_{total}) calculated at $P/P_0 \approx 0.99$. ^c Average pore diameter (D_{ave}).

XPS measurements were employed to analyze the components and chemical bondings at the surface of the carbon materials. The peaks of C 1s, N 1s, and O 1s were detected from the wide XPS survey spectrum. The high-resolution XPS spectra of C 1s, N 1s, and O 1s were collected to analyze the detailed information. The C 1s spectrum of PMC can be deconvoluted into five peaks located at 284.6, 285.9, 286.5, 287.6, and 288.8 eV (Fig. 2-4d), corresponding to aromatic and aliphatic carbon (C-C), hydroxyl and phenol groups (COR), carbon in keto-enol equilibria (C_{KE}), keto and quinone groups (C=O), and carboxylic groups (COOR), respectively. In the region of the N 1s core-level spectrum (Fig. 2-4e), the chemical states of the N atom, with binding energies of 398.3, 399.9 and 401.6 eV, can be identified as the pyridinic-N (N-6, ~34%), the pyrrolic-N (N-5, ~49%), and graphitic-N (N-G, ~17%), respectively.^{11, 12} Among them, N-5 and N-6 contribute to the pseudo-capacitance, while N-G promotes electron

transport and effectively enhances the conductivity of carbon materials. Four characteristic peaks in the O 1s spectrum were centered at 531.5 eV, 532.4 eV, 533.3 eV, and 534.2 eV (Fig. 2-4f).^{13, 14} These peaks were assigned to C=O groups (group 1), carbonyl oxygen atoms in esters, amides, anhydrides and carbonyl oxygen atoms in hydroxyls or ethers (group 2), the ether oxygen atoms in esters and anhydrides (group 3), and the oxygen atoms in carboxyl groups (group 4). The atomic contents of C, N and O species of PMC were calculated quantitatively as 86, 2.6, and 11 at%, respectively. The synergy of N-6, N-5 and N-G would contribute to the capacitance behaviour greatly with pseudo-capacitance.

Electrochemical measurements

To accurately evaluate the electrochemical performance, the PAN-based carbons as the SCs electrodes were investigated by CV and GC measurements in both three- and two-electrode systems. Firstly, the electrochemical capacity was tested in the potential window of 0-0.8 V under the three-electrode system and the results were shown in Fig. 2-5 and Fig. 2-6. Generally, an ideal electrochemically active electrode material shows a nearly rectangular CV shape.¹⁵ As shown in Fig. 2-5a, CD-PMC and PMC both displayed a quasi-rectangular CV shape at the scan rate of 5 mV s⁻¹, while PMC presented a larger integrated area, suggesting a higher specific capacitance.¹⁶ The CV curves of PMC tested at different scan rates were plotted in Fig. 2-5b. The CV curves remained a satisfactory rectangular shape up to 200 mV s⁻¹ indicating a typical electric double layer capacitive behavior, and that the PMC-based electrode was stable in 1 M H₂SO₄ aqueous electrolyte. Even at 500 mV s⁻¹, an approximately rectangular shape was maintained, which demonstrated a highly reversible adsorption/desorption of the electrolyte ions among the surface of the PMC electrode and indicated an excellent rate performance. It must be mentioned that the CV curves showed small humps in the range of 0.7 to 0.8 V, characteristic of faradaic pseudo-capacitance due to redox reactions, which may be attributed to N and O functional groups on the surface of PAN-based carbon.^{6, 17} Rate capability is considered as one key factor for the

application of carbon-based electrode materials. Fig. 2-5c showed the specific capacitances of CD-PMC and PMC as a function of scan rates. The specific capacitances were calculated from CV data by Eq. (2-1) at various scan rates ranging from 1 to 100 mV s^{-1} . It is well known that specific capacitance of electrode materials decreases with an increase of scan rate, which is attributed to ion diffusion limitation within the highly porous structure lags.¹⁸ As shown in Fig. 2-5c, PMC showed a much higher specific capacitance than CD-PMC, which may be due to its high specific surface area and suitable porous structures.¹⁹ Furthermore, the capacitance retention of PMC exhibited as high as 78% at the scan rate of 100 mV s^{-1} from 1 mV s^{-1} , demonstrating a quick ion transport capability and excellent rate performance.

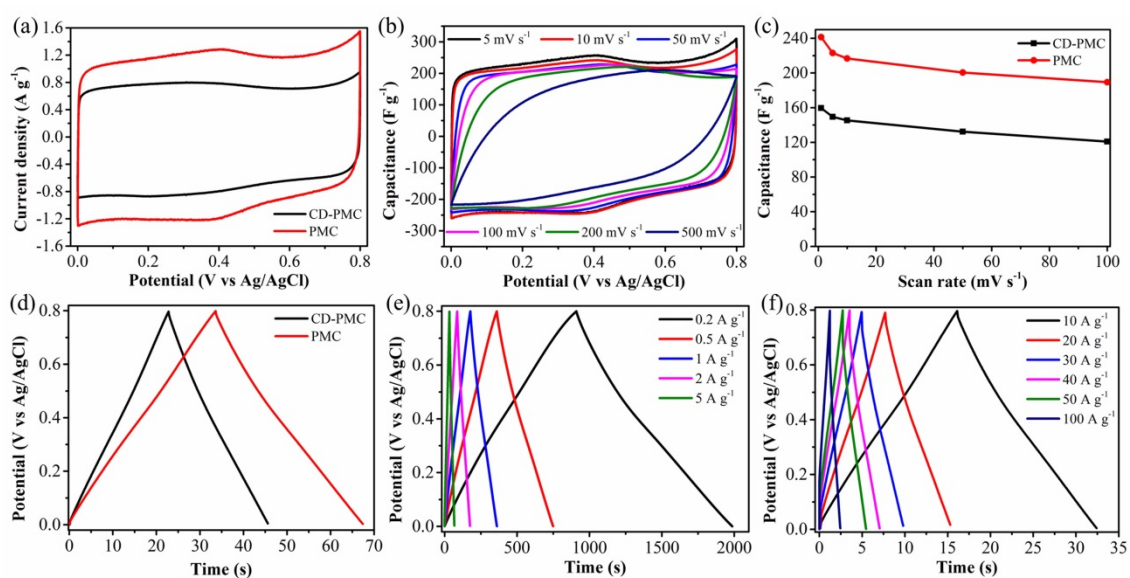


Figure 2-5. CV curves of CD-PMC and PMC at a scan rate of 5 mV s^{-1} (a), CV curves of PMC at scan rates varying from 5 to 500 mV s^{-1} (b), Comparison of specific capacitance as a function of scan rate for CD-PMC and PMC (c), GC curves of CD-PMC and PMC at a current density of 5 A g^{-1} (d), GC curves of PMC at current densities from 0.2 to 5 A g^{-1} (e) and 10 to 100 A g^{-1} (f).

The GC curves of CD-PMC and PMC measured in 1 M H_2SO_4 at a current density of 5 A g^{-1} were depicted in Fig. 2-5d. They both displayed a triangular shape which presented reversibility, an ideal electrical double-layer capacitive characteristic and high charge/discharge efficiency.²⁰ Generally, the longer the charge/discharge time

is, the more the electrolyte ions would participate in charge/discharge process, which leads to a high specific capacitance.²¹ In comparison with CD-PMC, PMC revealed a longer charge/discharge time and thus a higher specific capacitance. The GC curves of PMC remained linearity and symmetry very well at current densities varied from 0.2 to 5 A g⁻¹ (Fig. 2-5e). The typical isosceles triangular shape without obvious voltage drop related to the internal resistance represented an indication of excellent capacitive behavior of PMC. Even at high current densities from 10 to 100 A g⁻¹, the triangular shapes were maintained and a small voltage drop occurred (Fig. 2-5f). The charge/discharge time significantly decreased with an increase of current densities because the electrolyte ions had sufficient time to enter and diffuse into the pores at lower current densities.²²

The gravimetric specific capacitances at various current densities ranging from 0.2 A g⁻¹ to 100 A g⁻¹ were calculated by Eq. (2-2) and plotted in Fig. 2-6a. The specific capacitances of CD-PMC and PMC almost remained unchanged after 10 A g⁻¹, indicating the superior rate capability. In addition, PMC displayed the higher specific capacitance than CD-PMC. The specific capacitances of PMC were 270 F g⁻¹ at 0.2 A g⁻¹ and 195 F g⁻¹ even at a very high current density of 100 A g⁻¹, resulting in a high capacitance retention rate of 72%. Cycling stability is considered as another crucial factor in practical applications of the SCs. Therefore, PMC-based electrode was charged/discharged for 5000 cycles at a current density of 20 A g⁻¹ in the three-electrode system within a potential window of 0-0.8 V (Fig. 2-6b). As can be seen, there was only a small-scale change of capacitance retention with cycle number. Remarkably, PMC possessed the outstanding cycle durability with the high retention rate of nearly 100% after 5000 cycles. The gradually increased capacitance between 2500 to 5000 cycles could be possibly attributed to the improved wettability and activating process of this electrode, that is, the continuous diffusion of the electrolyte ions into the porosity would lead to the gradual increase in the effective charge storage sites of PMC-based electrode and thus the specific capacitance.²³ The GC curves of the first and last five cycles were

almost identical isosceles triangles, demonstrating an excellent long-term cycle stability of PMC (Fig. 2-6b, inset). EIS measurements were performed at room temperature in the 1 M H₂SO₄ electrolyte to explore the frequency response characteristics of PMC (Fig. 2-6c). The Nyquist plots of PMC-based electrode displayed a small semicircle and nearly vertical line, indicative of a low contact resistance and good capacitive response.

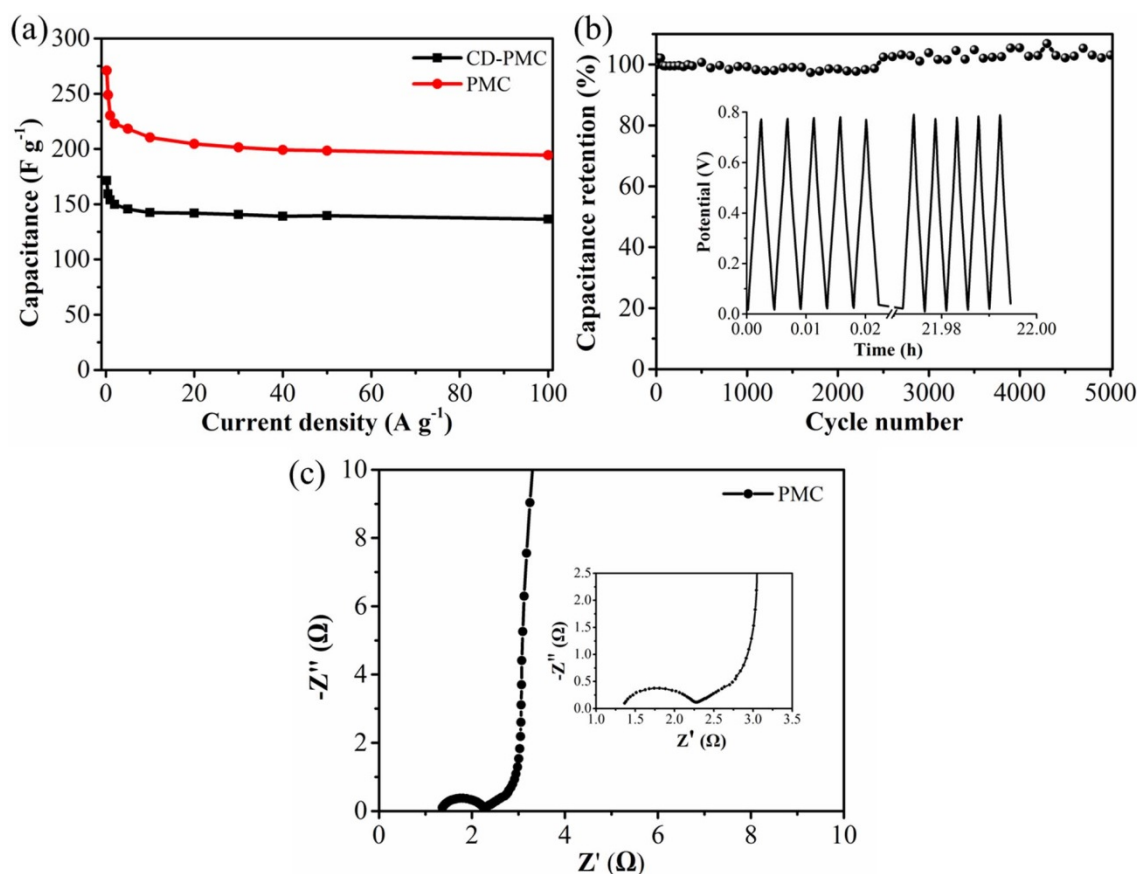


Figure 2-6. Comparison of specific capacitance as a function of current density for CD-PMC and PMC (a), Capacitance retention of PMC from GC curves at a constant current density of 20 A g⁻¹ for 5000 cycles with the first 5 and last 5 cycles inset (b), Nyquist plot of the PMC with the inset of enlarged high frequency region (c).

In order to further investigate the electrochemical capacitive practical performances for the PAN-based carbon electrodes, a symmetric SC was assembled with two nearly identical (weight and size) carbon films as the electrodes and 1 M H₂SO₄ aqueous solution as the electrolyte. For comparison, commercial activated

carbon (YP-50F) was also tested. Fig. 2-7a showed the CV curves of the three kinds of electrodes in the 1 M H₂SO₄ solution at the scan rate of 5 mV s⁻¹ and the operating voltage range of 0-1 V. It was obvious that CV curves exhibited relatively rectangular shape and PMC-based electrodes showed the largest integrated area, which was consistent with the results of that tested in the three-electrode system. In this assembled two-electrode cell, carbon-based electrodes were sufficiently dipped in the aqueous electrolyte solution and then directly used without the addition of electrolyte. Thus, the electrochemical performance of the SC was mainly determined by the properties of electrodes. The surface morphology of the electrode film was observed by SEM images (Fig. 2-8). The electrodes from CD-PMC and PMC showed a similar surface appearance. In addition, the capacitive behaviors of electrodes were also dependent on the wettability of the inner pores for the electrolyte.²⁴ Contact angle (CA) measurement was also carried out to study the surface wettability of all electrodes for 1 M H₂SO₄ aqueous electrolyte, which was used to preliminary evaluate the performance of the electrode for SCs (Fig. 2-8, inset).²⁵ PMC-based electrode gave a smaller CA value, which was in agreement with the larger CV integrated area, and thus a higher specific capacitance. The CV curves of PMC-based electrodes remained relatively rectangular shape at various scan rates from 5 to 500 mV s⁻¹, indicating a near-ideal capacitive behavior with good rate performance (Fig. 2-7b). The GC curves of three kinds of electrodes at the constant current density of 0.5 A g⁻¹ exhibited typical triangle shapes without obvious voltage drops, indicating excellent coulombic efficiency together with good double-layer capacitive performance (Fig. 2-7c). PMC-based SC showed the longest charge/discharge time, meaning the highest specific capacitance. The GC curves of PMC under current densities ranging from 0.1 to 1 A g⁻¹ were shown in Fig. 2-7d. All of the GC curves at different current densities exhibited good triangle-shapes and excellent coulomb efficient.

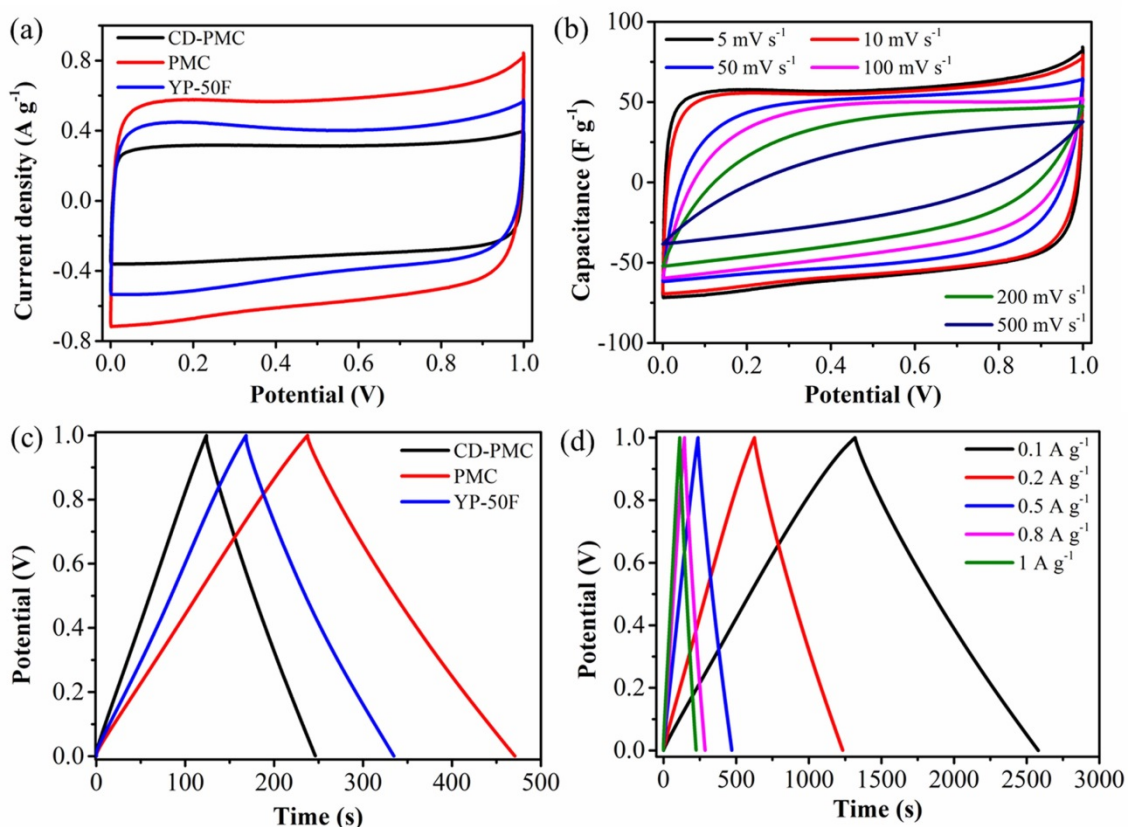


Figure 2-7. Electrochemical performance tested in a two-electrode system with a potential window of 0-1 V. CV curves of CD-PMC, PMC, and YP-50F at a scan rate of 5 mV s⁻¹ (a) and CV curves of PMC at scan rates from 5 to 500 mV s⁻¹ (b), GC curves of CD-PMC, PMC, and YP-50F at a current density of 0.5 A g⁻¹ (c) and GC curves of PMC at current densities from 0.1 to 1 A g⁻¹ (d).

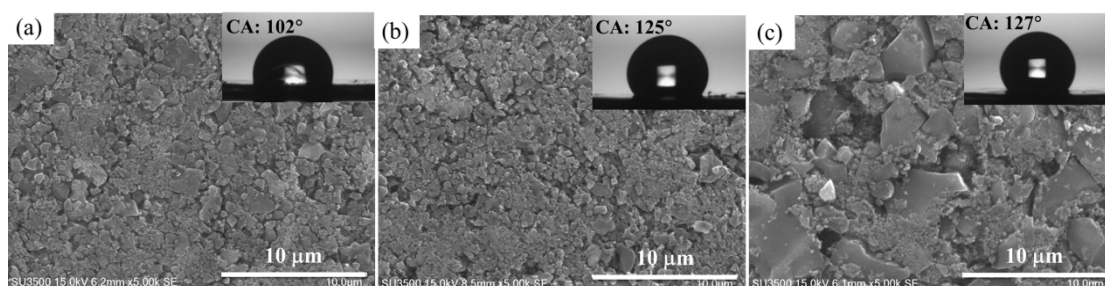


Figure 2-8. SEM images of electrode films synthesized by PMC (a), CD-PMC (b), and YP-50F (c) with the inset of contact angle results for 1 M H₂SO₄ aqueous electrolyte.

The relationships between the specific capacitance of the total symmetrical SC calculated from the discharge curves by Eq. (1-1) and the current densities were

summarized in Fig. 2-9a. The specific capacitance of PMC-based SC was as high as 63 F g⁻¹ at the current density of 0.1 A g⁻¹ and 40 F g⁻¹ even at the high current density of 20 A g⁻¹ (about 63% capacitance retention), which was obviously higher than the value of YP-50F-based SC.

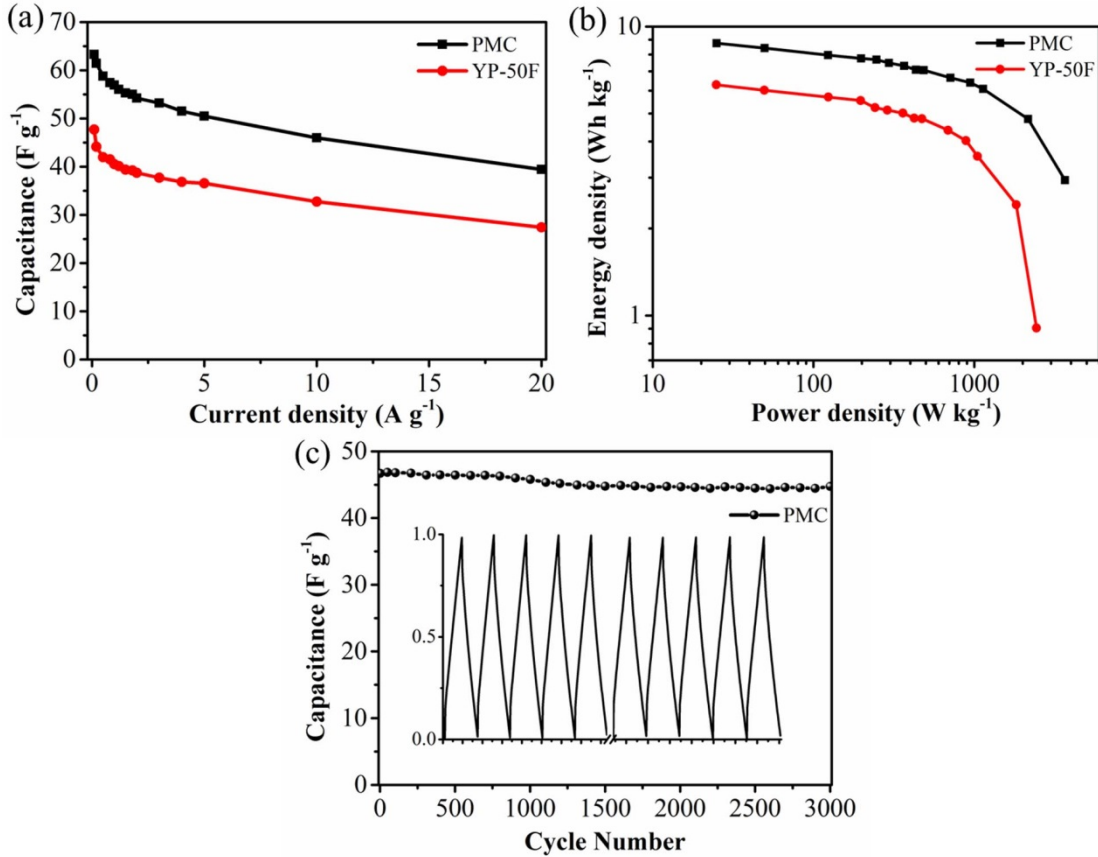


Figure 2-9. The total specific capacitances of the symmetrical SCs from PMC and YP-50F as a function of current density (a), Ragone plot referring to the energy and power density of PMC and YP-50F-based SCs (b), Capacitance retention of PMC-based SC from the GC curves at a constant current density of 10 A g⁻¹ for 3000 cycles with the first and last five cycles inset (c).

Furthermore, energy density and power density of the PMC-based SC were calculated by Eq. (1-2) and (1-3), respectively. And the Ragone plot was drawn in Fig. 2-9b. The energy density of the PMC-assembled SC decreased from 8.8 to 2.9 Wh kg⁻¹ with increasing of current density from 0.1 to 20 A g⁻¹, while the power density reached to 3666 from 25 W kg⁻¹. It was obvious that PMC-based SC possessed higher

energy/power densities than the commercial carbon. Finally, the cycling performance of PMC-based SC was also evaluated using the GC and shown in Fig. 2-9c. The specific capacitance remained at 47 F g⁻¹ for the first cycle and 45 F g⁻¹ for the 3000 cycles with the retention of 96%, indicating that the charge/discharge process of PMC-assembled SC was highly reversible. The almost similar GC curves of the first five cycles and the last five cycles also indicated the good cycling and stability behaviors of PMC as the SC electrodes (Fig. 2-9c. inset). Comparison with other reported carbons derived from PAN or its composites, as shown in Table 2-2, PMC herein demonstrated the desired specific capacitance, excellent rate capacitance and cycle stability not only in the three-electrode system but also in the symmetrical SC.

Table 2-2. Comparison of the electrochemical performance of PAN-based carbons for supercapacitors reported in the literature.

| Precursor | S _{BET} (m ² g ⁻¹) | Electrolyte | Cell ^c | Capacitance (F g ⁻¹) | Rate capacitance | Cycle stability |
|--------------------------|---|------------------------------------|-------------------|-------------------------------------|---------------------------------------|--------------------|
| PAN ²⁶ | 722 | 1 M H ₂ SO ₄ | 3E | 108 at 0.05 A g ⁻¹ | 50% from 0.05 to 20 A g ⁻¹ | – |
| PAN/APEG ²⁷ | 753 | 6 M KOH | 2E | 302 at 0.2 A g ⁻¹ | 56% from 0.2 to 40 A g ⁻¹ | 94.6% |
| PAN-b-PMMA ²⁸ | 403 | 2 M KOH | 3E | 314 at 0.5 A g ⁻¹ | 68% from 0.5 to 20 A g ⁻¹ | 90% |
| | | | 2E | 210 at 0.5 A g ⁻¹ | 58% from 0.5 to 10 A g ⁻¹ | – |
| PAN ²⁹ | 1165 | 6 M KOH | 3E | 167 at 30 mV s ⁻¹ | 67% from 0.75 to 6 A g ⁻¹ | 78% |
| PAN ³⁰ | 3550 | Organic ^a | 2E | 216 at 0.05 A g ⁻¹ | 56% from 0.05 to 10 A g ⁻¹ | 100% |
| PAN/CNT ³¹ | 613.8 | 1 M H ₂ SO ₄ | 3E | 216 at 10 mV s ⁻¹ | 63% from 10 to 200 mV s ⁻¹ | 100% |
| PAN/PANI ³² | 410 | 1 M H ₂ SO ₄ | 3E | 335 at 0.5 A g ⁻¹ | 52% from 0.5 to 32 A g ⁻¹ | – |
| | | | 2E | – | – | 86% |
| PAN ¹⁰ | 3130 | Organic ^b | 2E | 181 at 1 A g ⁻¹ | 77% from 1 to 10 A g ⁻¹ | 96% |
| PMMA/PAN ⁶ | 2085 | 6 M KOH | 3E | 314 at 0.5 A g ⁻¹ | 83% from 1 to 20 A g ⁻¹ | 96% |
| PAN | 1600 | 1 M H ₂ SO ₄ | 3E | 270 at 0.2 A g ⁻¹ | 72% from 0.2 to 100 A g ⁻¹ | 100% |
| (This chapter) | | | 2E | 253 at 0.1 A g ⁻¹ | 62% from 0.1 to 20 A g ⁻¹ | 96% |

^a 1 M LiPF₆ in EC/DMC: 1 M of LiPF₆ in a mixture of ethylene carbonate (EC) and dimethyl carbonate (DMC) (3:7 volume ratio). ^b EMImBF₄: ethyl-3-methylimidazolium tetrafluoroborate. ^c 3E: three-electrode system; 2E: two-electrode system.

2.4 Conclusion

In this chapter, the author displayed a facile route for synthesis of N-doped and shape-controlled porous monolithic carbons from PAN *via* a template-free approach followed by an easy pyrolysis process. And their applications as SC electrode materials were discussed. Two typical activation methods were employed to prepare PMC with the advantages of large surface area, suitable pore size distribution, and high nitrogen content. Subsequently, the electrochemical performance was evaluated by CV and GC measurements in both three- and two-electrode systems. PMC-based SC tested in a three-electrode system exhibited the high capacitance of 270 F g⁻¹ at 0.2 A g⁻¹ and 195 F g⁻¹ at 100 A g⁻¹, the excellent capacitance retention of 72% from 0.2 to 100 A g⁻¹, the outstanding cycling stability with no capacitance decay at 20 A g⁻¹ after 5000 cycles. In addition, the symmetric SC from PMC also showed the high specific capacitance of 63 F g⁻¹ at 0.1 A g⁻¹ and superior cycle stability with the retention of 96% after 3000 cycles. The results demonstrated that the obtained PMC is a highly promising electrode material for high performance supercapacitors. Furthermore, the facile and efficient route for N-doped and shape-controlled porous carbons can be readily extended to other types of nitrogen-containing polymer sources.

2.5 References

1. P. Chen, L. Wang, G. Wang, M. Gao, J. Ge, W. Yuan, Y. Shen, A. Xie and S. Yu, *Energy Environ. Sci.*, 2014, **7**, 4095-4103.
2. J. Li, K. Li, M. Li, D. Gosselink, Y. Zhang and P. Chen, *J. Power Sources*, 2014, **252**, 107-112.
3. Y. Deng, Y. Xie, K. Zou and X. Ji, *J. Mater. Chem. A*, 2016, **4**, 1144-1173.
4. L. F. Chen, X. D. Zhang, H. W. Liang, M. Kong, Q. F. Guan, P. Chen, Z. Y. Wu and S. H. Yu, *ACS Nano*, 2012, **6**, 7092-7102.

5. X. Zhang, L. Ma, M. Gan, G. Fu, M. Jin, Y. Lei, P. Yang and M. Yan, *J. Power Sources*, 2017, **340**, 22-31.
6. L. Yao, G. Yang, P. Han, Z. Tang and J. Yang, *J. Power Sources*, 2016, **315**, 209-217.
7. S. Lei, W. Cao, Z. Fu and L. Xu, *J. Appl. Polym. Sci.*, 2016, **133**, 43890.
8. M. S. A. Rahaman, A. F. Ismail and A. Mustafa, *Polym. Degrad. Stab.*, 2007, **92**, 1421-1432.
9. A. Palanisamy, N. V. Salim, B. L. Fox, P. Jyotishkumar, T. Pradeep and N. Hameed, *RSC Adv.*, 2016, **6**, 55792-55799.
10. L. Yao, G. Yang and P. Han, *RSC Adv.*, 2016, **6**, 43748-43754.
11. J. M. Jiménez Mateos, J. L. G. Fierro, *Surf. Interface Anal.*, 1996, **24**, 223-236.
12. J. Casanovas, J. M. Ricart, J. Rubio, F. Illas, J. M. Jiménez-Mateos, *J. Am. Chem. Soc.*, 1996, **118**, 8071-8076.
13. J. Maruyama, M. Umemura, M. Inaba, A. Tasaka, I. Abe, *J. Electrochem. Soc.*, 2009, **156**, A181-A186.
14. U. Zielke, K. J. Hüttinger, W. P. Hoffman, *Carbon*, 1996, **34**, 983-998.
15. Q. Wang, J. Yan, Y. Wang, T. Wei, M. Zhang, X. Jing and Z. Fan, *Carbon*, 2014, **67**, 119-127.
16. J. Yan, Q. Wang, C. Lin, T. Wei and Z. Fan, *Adv. Energy Mater.*, 2014, **4**, 1400500.
17. A. Choudhury, J. H. Kim, S. Sinha Mahapatra, K. S. Yang and D. J. Yang, *ACS Sustainable Chem. Eng.*, 2017, **5**, 2109-2118.
18. G. Zu, J. Shen, L. Zou, F. Wang, X. Wang, Y. Zhang and X. Yao, *Carbon*, 2016, **99**, 203-211.
19. X. Hao, J. Wang, B. Ding, Y. Wang, Z. Chang, H. Dou and X. Zhang, *J. Power Sources*, 2017, **352**, 34-41.
20. Q. Liang, L. Ye, Z.H. Huang, Q. Xu, Y. Bai, F. Kang and Q.H. Yang, *Nanoscale*, 2014, **6**, 13831-13837.

21. X. Gao, W. Xing, J. Zhou, G. Wang, S. Zhuo, Z. Liu, Q. Xue and Z. Yan, *Electrochim. Acta*, 2014, **133**, 459-466.
22. G. Ma, Q. Yang, K. Sun, H. Peng, F. Ran, X. Zhao and Z. Lei, *Bioresour. Technol.*, 2015, **197**, 137-142.
23. J. Zhou, J. Lian, L. Hou, J. Zhang, H. Gou, M. Xia, Y. Zhao, T.A. Strobel, L. Tao and F. Gao, *Nat. Commun.*, 2015, **6**, 8503.
24. D. G. Gromadskyi, J. H. Chae, S. A. Norman and G. Z. Chen, *Appl. Energy*, 2015, **159**, 39-50.
25. M. M. Vadiyar, S. C. Bhise, S. K. Patil, S. S. Kolekar, A. R. Shelke, N. G. Deshpande, J. Y. Chang, K. S. Ghule and A. V. Ghule, *Chem. Commun.*, 2016, **52**, 2557-2560.
26. H. Tenmyo, T. Asano, Y. Jo, K. Yoshii, T. Tsuda, J. Maruyama, H. Uyama and S. Kuwabata, *Electrochemistry*, 2015, **83**, 348-350.
27. K. Huang, M. Li, Z. Chen, Y. Yao and X. Yang, *Electrochim. Acta*, 2015, **158**, 306-313.
28. K. Yan, L. B. Kong, K. W. Shen, Y. H. Dai, M. Shi, B. Hu, Y. C. Luo and L. Kang, *Appl. Surf. Sci.*, 2016, **364**, 850-861.
29. Y. Xu, J. Sun, H. Chen and L. Bai, *RSC Adv.*, 2015, **5**, 37780-37788.
30. K. Gupta, T. Liu, R. Kaviani, H. G. Chae, G. H. Ryu, Z. Lee, S. W. Lee and S. Kumar, *J. Mater. Chem. A*, 2016, **4**, 18294-18299.
31. Y. Wang, B. Fugetsu, Z. Wang, W. Gong, I. Sakata, S. Morimoto, Y. Hashimoto, M. Endo, M. Dresselhaus and M. Terrones, *Sci. Rep.*, 2017, **7**, 40259.
32. F. Miao, C. Shao, X. Li, K. Wang and Y. Liu, *J. Mater. Chem. A*, 2016, **4**, 4180-4187.

Chapter 3

Novel porous carbon from biomass/polymer composite for high performance supercapacitor

3.1 Introduction

Nowadays, N-enriched hierarchically porous carbons are considered as the optimum candidates for supercapacitors (SCs) application.¹⁻³ The combination of the electrical double-layer capacitance and pseudo-capacitance presents an effective approach to improve the overall capacitance and conductivity without destroying the electrochemical stability and high rate property.^{4, 5} Thus, the study on N-doped hierarchically porous carbons has aroused extremely interest in the field of energy storage.

As described in chapter 1, hierarchically porous activated carbons (ACs) derived from apricot shell (AS) were prepared through a green steam activation method. And the AS-based AC (ASAC) displayed a good electrochemical performance in a symmetrical SC system. In chapter 2, the fabrication route for the N-doped and shape-controlled porous monolithic carbons (PMC) derived from polyacrylonitrile (PAN) was demonstrated. PMC possessed large surface area and high N content were prepared through a template-free thermally induced phase separation (TIPS) approach followed by a KOH activation. Furthermore, PMC displayed an excellent electrochemical performance on both three- and two-electrode systems. Inspired by the advantages of ASAC and PMC, the synthetic route for novel N-doped porous monolithic carbon (NDPMC) from the composite of biomass and polymer was designed.

In this chapter, the author employs ASAC as a minor electrode component to improve the electrical conductivity and mechanical properties of the composite. PAN is a very suitable polymer precursor to prepare a mesoporous monolith with high nitrogen

content *via* TIPS technique because of its good processability and low price, which further promote to obtain an electrochemically active carbon matrix containing a certain amount of nitrogen. The 3D ASAC/PAN composite monolith was firstly fabricated as the starting material through the template-free TIPS approach. After the stabilization and KOH activation process, the NDPMC was obtained and displayed a high specific surface area, hierarchical porous distribution, and uniform nitrogen content. The electrochemical performance of NDPMC was systematically evaluated in both three-electrode and the practical symmetrical system. To the best of my knowledge, this is the first report of synthesis of N-doped porous monolithic carbon by combining biomass-based carbon with N-containing polymer and its applications in electrodes for SCs.

3.2 Experimental

Materials

Polyacrylonitrile copolymer (PAN) was obtained from Mitsubishi Rayon Co. Ltd. Apricot shell was supported by farmers of Baoji city (Shaanxi Province, China). Apricot shell-based activated carbon (ASAC) was prepared by steam activation which was carried out in a rotary tube furnace at 950 °C for 3 h. ASAC exhibited a BET surface area of 1770 m² g⁻¹, pore volume of 1.16 cm³ g⁻¹, and average pore diameter of 2.6 nm. Elemental analysis of ASAC conducted by a CHN Corder showed 77.3, 1.06, and 0.12% for C, H, and N contents, respectively. The particle size of ASAC used in this study was less than 45 μm.

Fabrication of composite monoliths

A three-dimensional (3D) porous composite monolith was manufactured by combining ASAC with PAN under a certain weight ratio through the template-free TIPS approach. At first, ASAC (0.042 g) was dispersed in *N,N*-dimethylformamide (DMF, 5.1 mL) by ultrasonication for 30 min, then PAN (0.42 g) was added to the

ASAC/DMF suspension and the whole mixture was further ultrasonicated for another 30 min. Subsequently, the mixture solution was heated and stirred at 85 °C and deionized water (0.9 mL) was added drop by drop. After PAN became completely dissolved, the solution was cooled at 25 °C for phase separation. The formed gel was immersed in methanol under mild shaking for removing DMF. Finally, the N-doped porous monolith (NDPM) with 10 wt% ASAC was obtained by drying under reduced vacuum for one day. Various composite monoliths were fabricated by increasing the weight ratio of ASAC and PAN.

Preparation of N-doped porous monolithic carbon

At first, NDPM was subjected to oxidative stabilization by heating at 230 °C for 6 h under air. Then, the stabilized N-doped porous composite monolith (SNDPM) was calcined at 600 °C for 1 h under an argon atmosphere to obtain the carbonized N-doped porous monolith (CNDPM). In order to mix with KOH reagent thoroughly, CNDPM was crushed for the further activation process. Subsequently, KOH activation was performed as follows: a given mass of CNDPM was blended using KOH (CNDPM/KOH mass ratio: 1/1), and the mixture was heated at 200 °C, 500 °C, and finally at 800 °C for 1 h of each step in a furnace under the protection of N₂ flow. After cooling down to room temperature, the sample was neutralized by 1M HCl until a pH of 7 was reached and washed by deionized water for several times. Finally, the sample was dried at 105 °C for 1 day, which was denoted as NDPMC.

Characterization

The detailed techniques and instruments for SEM, TG analysis, FTIR, porosity property, EDX, element analysis, XRD, and XPS measurements were described in chapter 1. Raman spectra were scanned from 1900 to 900 cm⁻¹ using an NRS-3100 spectrometer (JASCO) equipped with an Ar⁺ ion laser ($\lambda=532.05$ nm, 0.3 mW) as the excitation source.

Electrochemical measurements

The electrochemical performance was evaluated in both the three- and two-electrode configurations by cyclic voltammetry (CV) and galvanostatic charge/discharge (GC) measurements with 1 M H₂SO₄ aqueous as electrolyte. All electrochemical measurements were carried out by using a CHI7002E electrochemical instrument (BAS Inc. ALS 7002E) at an ambient temperature. The detailed cell assembly and the performance evaluation were similar to the descriptions appeared in chapter 1 and chapter 2.

3.3 Results and Discussion

Properties of the composite monoliths

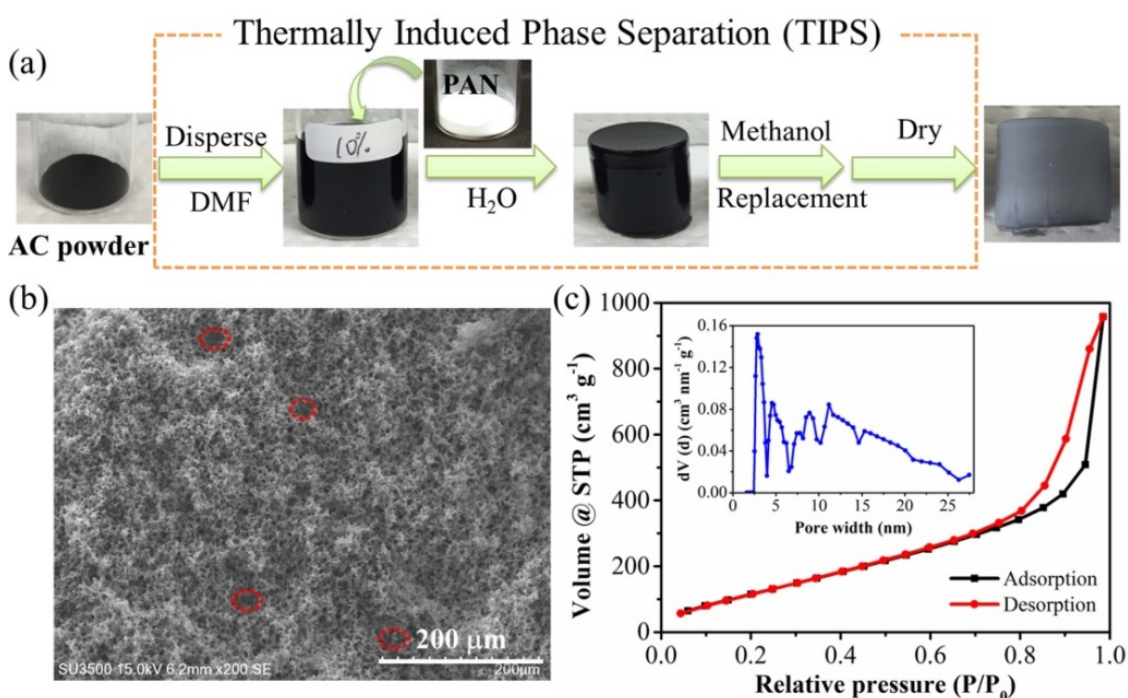


Figure 3-1. Facile route for fabrication of NDPM with 10 wt% ASAC by a TIPS approach (a), SEM image of NDPM with ASAC powder wrapped and ASAC distribution marked as red circles (b), Nitrogen adsorption/desorption isotherms and pore size distribution calculated by DFT method (inset) of NDPM (c).

The fabrication process of the composite monolith was shown in Fig. 3-1a. The scanning electron microscopy (SEM) image revealed that N-doped porous monolith (NDPM) displayed a three-dimensional (3D) porous structure and ASAC was found to be uniformly dispersed and distributed across the PAN matrix (Fig. 3-1b). The nitrogen adsorption/desorption isotherms of NDPM followed a typical type III isotherm with a large hysteresis loop at high relative pressure (Fig. 3-1c). The obtained NDPM showed a higher BET surface area of $530 \text{ m}^2 \text{ g}^{-1}$ with a pore volume of $1.46 \text{ cm}^3 \text{ g}^{-1}$ in comparison to the pure PAN monolith (Table 3-1) or a composite monolith of PAN and carbon nanotube.^{6,7} The pore size distribution calculated by the DFT method indicated the pore size of NDPM was mainly distributed into 2-25 nm (Fig. 3-1c, inset). The micropore (0-2 nm) and mesopore size (2-100 nm) distributions were depicted by HK and BJH models, respectively (Fig. 3-2). The pore size distribution of NDPM exhibited a hierarchically porous structure including a few micropores, abundant mesopores and macropores. Meanwhile, the microstructure and characters of the NDPM with ASAC loading ratios in the range from 5 to 30 wt%, for example, 10 wt% ASAC means ASAC: PAN=10/100, were also investigated.

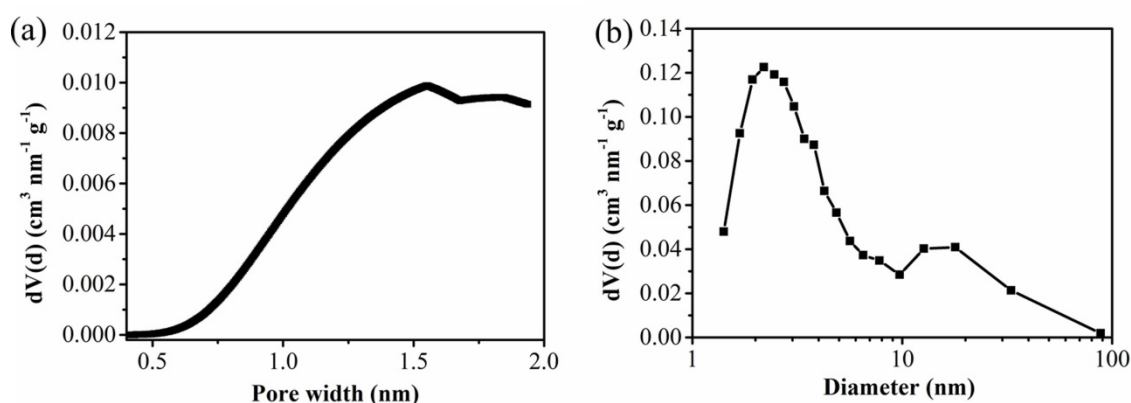


Figure 3-2. Pore size distribution calculated by HK (a) and BJH methods (b) of NDPM.

The surface morphologies of the fabricated monoliths were observed by SEM images and they all displayed a 3D porous structure (Fig. 3-3). However, the 3D network shrinkage appeared when the ASAC content was more than 30 wt%. The surface elemental compositions of the composite samples were captured by EDX

spectroscopy. It can be inferred that these composites mainly contained C, N, and O elements. The N and O contents of 10 wt% ASAC-PAN composite monolith were 25 wt% and 5.1 wt%, respectively (Table 3-1). The fabricated composite monoliths possessed the advantages of 3D hierarchical porous structure and enriched heteroatoms contents, endowing them with the great potential to prepare porous carbons with large surface area, uniform pore distribution, and high nitrogen content.

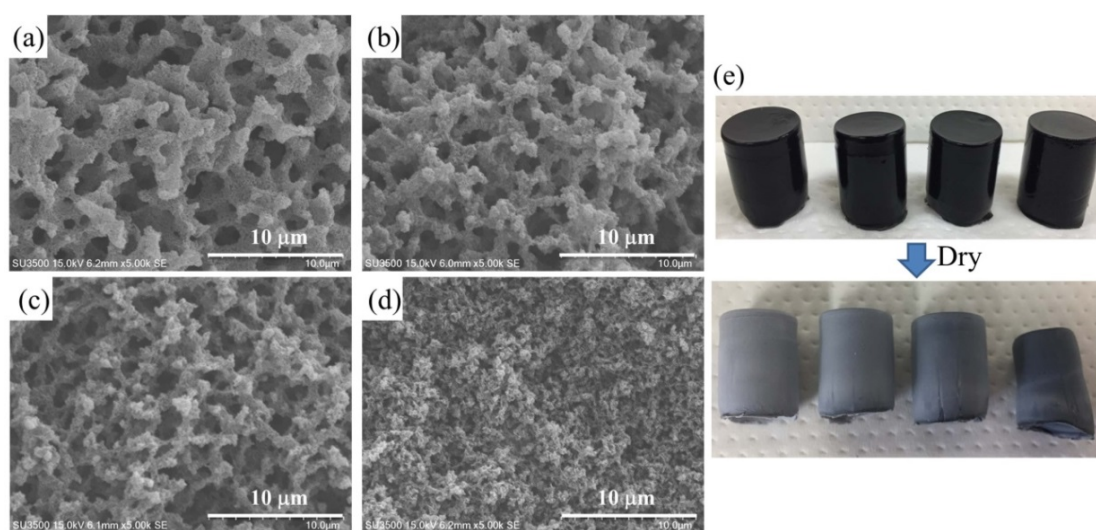


Figure 3-3. SEM images of composite monoliths fabricated by various ASAC/PAN weight ratios of (a) 5 wt%, (b) 10 wt%, (c) 15 wt%, and (d) 30 wt%; (e) photographs of the composite monoliths before (upper) and after (bottom) dry, in which ASAC weight increased from left to right.

Thermal degradation behaviors of the composite monoliths were studied using thermogravimetric (TG) analyzer (Fig. 3-4). It can be seen that there was almost no mass loss between 40-550 °C for ASAC. The dramatic weight loss of the composite samples occurred from 300 to 450 °C, indicating volatile gases came out and significant chemical reactions took place.⁸ Two distinct mass losses were observed at 320 °C and 415 °C from the DTG curve (Fig. 3-4b). The first mass loss began around 306 °C and the loss rate was about 15% in the range of 306-336 °C, which was associated with the production of volatile products, such as NH₃, HCN, or CH₃CN.⁹ The second stage occurred at 336-450 °C with the mass loss of ~20%, which was related to the thermal

degradation reactions of PAN. The resulting weight residues were about 63% at 500 °C for these composite monoliths except 5 wt% ASAC in which the weight residue was 55%. Obviously, the introduction of ASAC into these composite monoliths resulted in a higher total weight residue than that of pure PAN monolith (~50%), which was recognized to benefit to get higher product yield during the further activation process.

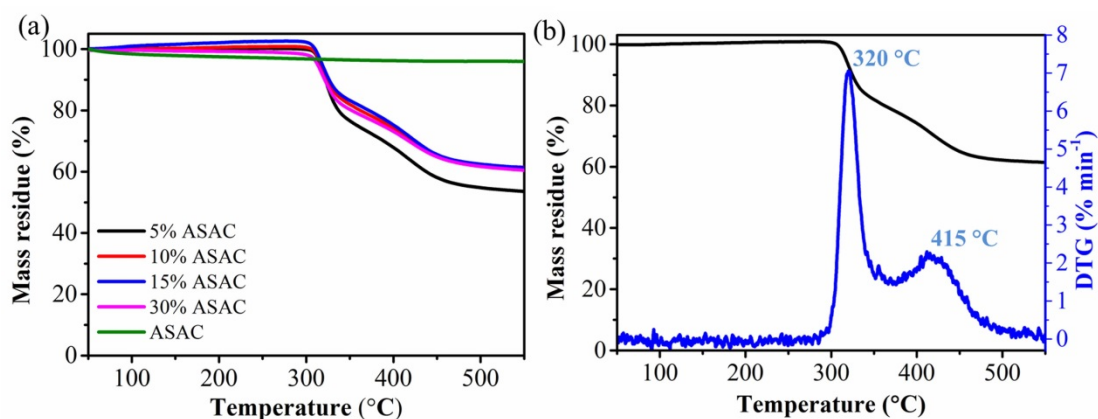


Figure 3-4. TG curves of ASAC and the composite monolith with different ASAC weight ratios (a), TG and DTG curves of 10 wt% ASAC composite monolith (b).

Generally, two thermal treatment steps including stabilization and carbonization are necessary for the production of PAN-based carbon which consists of pseudo-graphite microcrystal.¹⁰ Thus, NDPM were firstly stabilized at 230 °C for 6 h under air to get the stabilized NDPM (SNDPM). SEM images of SNDPM still remained a 3D porous structure (Fig. 3-5). The primary reactions including oxidation, dehydrogenation, and cyclization were speculated by FTIR spectra (Fig. 3-6). The dramatic decrease in 2250 cm⁻¹ (C≡N band) and obvious increase in 1590 cm⁻¹ (C=N band) compared with that of composite monoliths, which can be interpreted by the cyclization of -C≡N with forming of C=N.¹¹ The appearance of a small bond at 810 cm⁻¹ corresponded to C=C-H stretching vibration revealed the dehydrogenation and subsequent isomerization of NDPM during this stabilization process.¹² Furthermore, N content from EDX spectra almost remained constant after stabilization process. These results indicate that the stabilization of PAN proceeded even in the presence of ASAC.

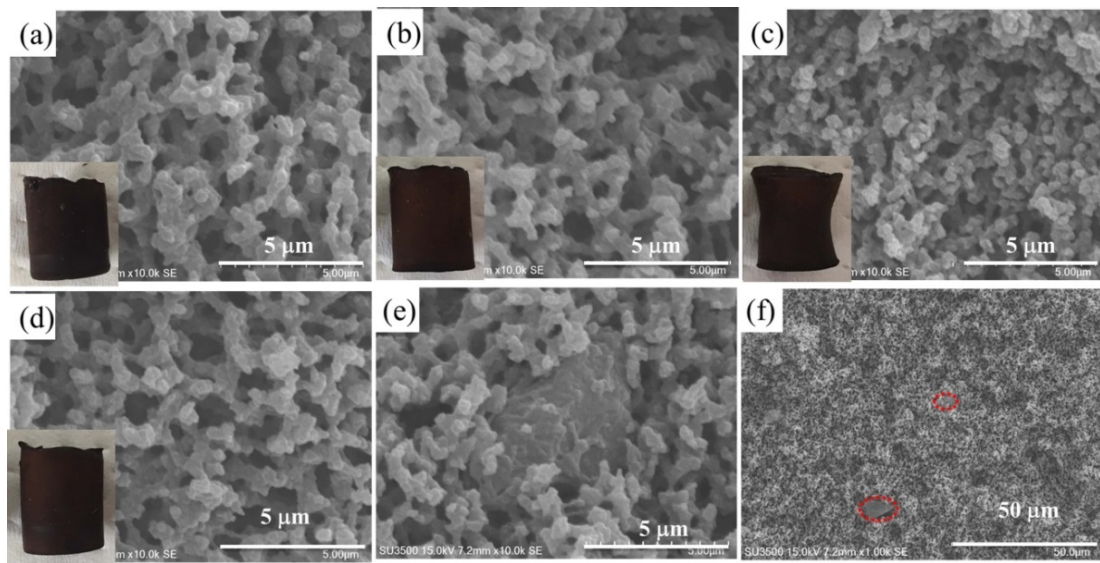


Figure 3-5. SEM images with photos inset of the stabilized composite monolith fabricated by various ASAC/PAN weight ratios of (a) 5 wt%, (b) 15 wt%, (c) 30 wt%, and (d) 10 wt%; (e) ASAC wrapped in 10 wt% sample; (f) low magnification of 10 wt% sample with ASAC marked as red circles.

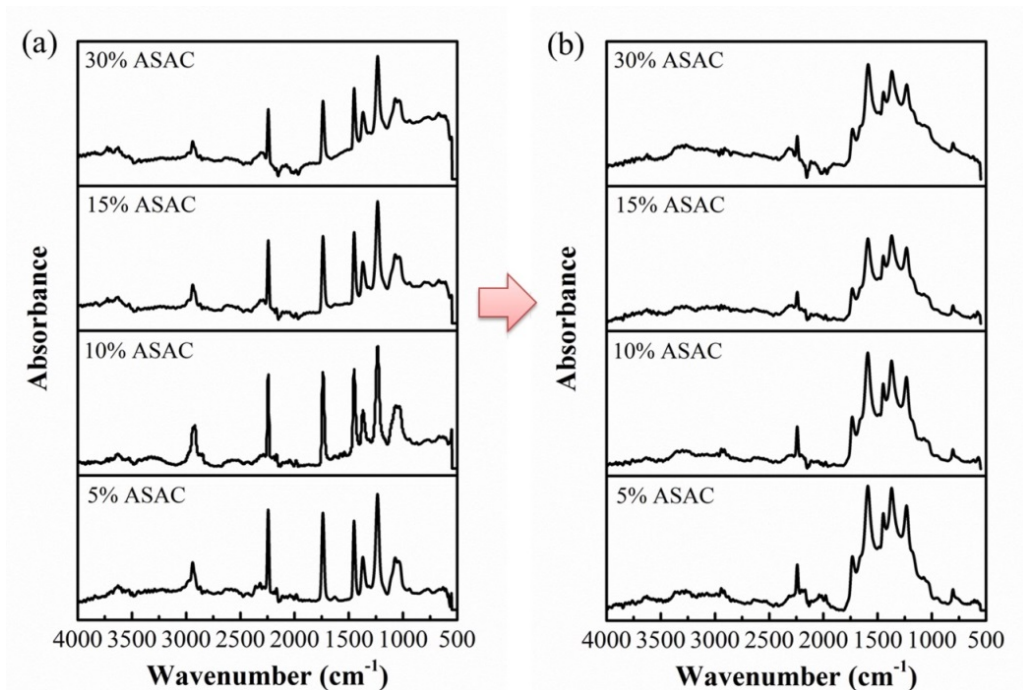


Figure 3-6. FTIR spectra of the composite monolith before (a) and after (b) stabilization process.

Characterization of the monolithic carbon

According to the above discussions, 3D network of composite monolith shrinkage appeared when the ASAC content was more than 30 wt% and that of 5 wt% may bring in a low product yield. Thus, 10 wt% ASAC was chose as the suitable activated carbon source in the further experiments. After the stabilization, SNDPM was carbonized and activated simultaneously under an equal weight of KOH to prepare N-doped porous monolithic carbon (NDPMC).

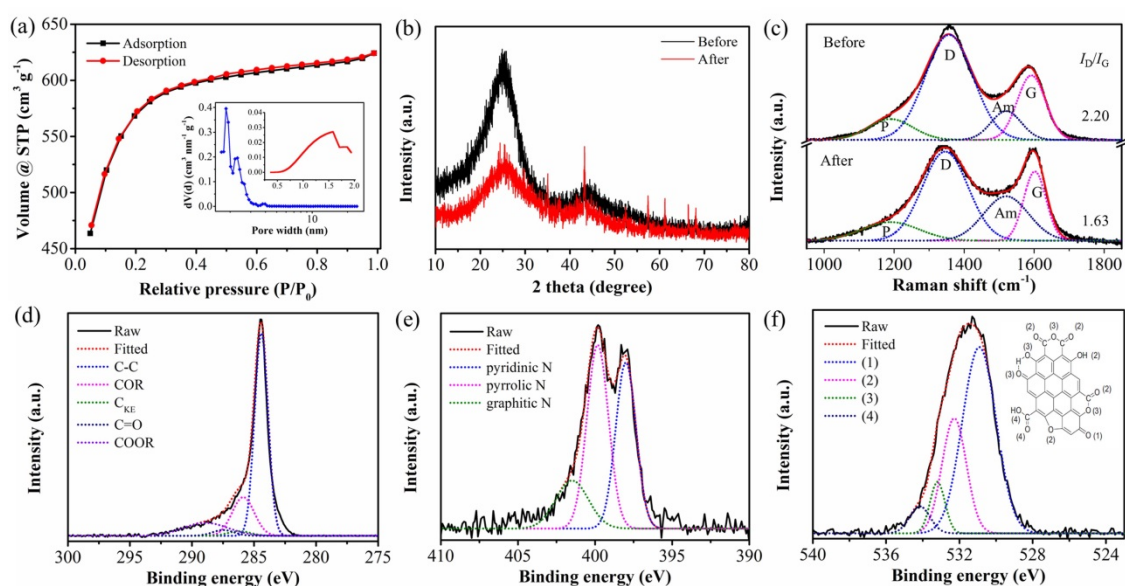


Figure 3-7. (a) Nitrogen adsorption/desorption isotherms and pore size distribution of NDPMC (inset, blue: DFT method; red: HK method), XRD patterns (b) and Raman spectra (c) of the samples before (CNDPM) and after (NDPMC) KOH activation, High-resolution XPS spectra and fitted data of C 1s peak (d), N 1s peak (e), and O 1s peak (f) for NDPMC.

The nitrogen adsorption/desorption isotherms and pore size distribution were illustrated to analyze the porosity properties of NDPMC (Fig. 3-7a). NDPMC exhibited a type-I isotherm and a small hysteresis loop occurred, corresponding to a complex mixture of micro and mesoporous structure. The pore size of NDPMC was mostly smaller than 5 nm from DFT method and micropore size calculated by HK method was mainly distributed between 0.5 to 2 nm with a peak around 1.7 nm. The specific surface

area measured by BET method was $1790 \text{ m}^2 \text{ g}^{-1}$, which was much higher than that of the fabricated composite monolith. Elemental analysis of NDPMC conducted by a CHN Corder showed 82, 0.8, and 8% for C, H, and N contents, respectively. In comparison with individual ASAC and pure PAN-based NDPMC (Table 3-1), the composite NDPMC possessed the merits of large surface area and high N content, which would be beneficial to promote the electrochemical properties of SCs, such as capacitance, rate capability, and cycling stability.

Table 3-1. BET surface area, pore volume, average pore diameter, and element analysis of all samples.

| Sample | From N ₂ adsorption at 77 K | | | | From CHN Corder | | | |
|-----------------------|--|---|---|---------------------------------------|-----------------|----------|----------|-------------------------|
| | S _{BET} ^a (m ² g ⁻¹) | V _{total} ^b (cm ³ g ⁻¹) | V _{micro} ^c (cm ³ g ⁻¹) | D _{ave} ^d (nm) | C (%) | H (%) | N (%) | O ^e (wt%) |
| ASAC | 1770 | 1.16 | 0.80 | 2.62 | 77.3 | 1.06 | 0.12 | - |
| NDPM ^e | 530 | 1.49 | 0.15 | 11.2 | 70 | - | 25 | 5.1 |
| NDPMC | 1790 | 0.96 | 0.84 | 2.15 | 82.4 | 0.78 | 7.96 | 6.3 |
| PAN-PM ^{e,f} | 188 | 0.71 | 0.07 | 15.1 | 67 | - | 27 | 5.9 |
| PAN-PMC ^g | 1600 | 0.862 | 0.74 | 2.16 | 80 | 0.53 | 5.63 | 6.0 |
| YP-50F | 1154 | 0.69 | 0.59 | 2.40 | - | - | - | - |

^a S_{BET} calculated by BET method. ^b Total pore volume (V_{total}) calculated at $P/P_0 \approx 0.99$. ^c Micropore volume calculated by HK method. ^d Average pore diameter (D_{ave}). ^e Surface chemical composition from EDX (wt%). ^f N-doped porous monolith derived from PAN without ASAC. ^g N-doped monolithic carbon derived from PAN without ASAC prepared under a same condition.

Fig. 3-7b showed XRD patterns of the samples before (carbonized sample, CNDPM) and after (NDPMC) activation process. Two characteristic peaks at $\sim 25^\circ$ and $\sim 43^\circ$ were observed, which corresponded to the (002) and (001) diffractions, respectively. It can be found that the intensity of (002) peak decreased after KOH activation, indicating a large number of amorphous structure with high specific surface area was formed. The structural disorder of the samples was investigated by using

Raman spectroscopy (Fig. 3-7c). The Raman spectrum was deconvoluted into four components; that is, the graphitic peak (G peak) at 1600 to 1620 cm^{-1} ; the disorder peak (D peak) at 1325 to 1355 cm^{-1} ; the peak ascribed to amorphous carbon (Am peak) at 1521 cm^{-1} ; and the peak ascribed to sp^3 -bonded carbon atoms (P peak) at 1185 cm^{-1} .¹³ The internal intensity ratio of D band and G band (I_D/I_G) obtained by fitting the spectra is known to be used as an indicator of the degree of graphitization, and the smaller I_D/I_G value means the higher degree of graphitization. The value of I_D/I_G was determined to be 1.63 for NDPMC. The value was lower than that before the KOH activation due to the retention of the carbon matrix with higher degree of graphitization, which might be beneficial for the electron conduction and high power output as electrode materials for SCs.

XPS measurements were employed to analyze the components and chemical bonding at the surface of the samples before and after KOH activation. The peaks of C 1s, N 1s, and O 1s were detected. To obtain the detailed information, the high-resolution XPS spectra of C 1s, N 1s, and O 1s were collected (Fig. 3-7d-f). The C 1s spectrum of NDPMC was deconvoluted into five peaks (Fig. 3-7d), which corresponded to aromatic and aliphatic carbon at 284.4 eV (C-C), hydroxyl and phenol groups at 285.9 eV (COR), carbon in keto-enol equilibria at 286.2 eV (C_{KE}), keto and quinone groups at 287.6 eV (C=O), and carboxylic groups at 289.1 eV (COOR). In the region of the N 1s core-level spectrum (Fig. 3-7e), the chemical states of the N atom, with binding energies of 398.1, 399.8 and 401.5 eV, can be identified as the pyridinic-N (N-6, ~37.8 at%), the pyrrolic-N (N-5, ~44.6 at%), and graphitic-N (N-G, ~17.5 at%), respectively.^{14, 15} Among them, N-5 and N-6 contribute to the pseudo-capacitance, while N-G promotes electron transport and effectively enhances the conductivity of carbon materials.² Four characteristic peaks in the O 1s spectrum (Fig. 3-7f) were centered at 531.5 eV, 532.4 eV, 533.3 eV, and 534.2 eV.^{16, 17} These peaks were assigned to C=O groups (group 1), carbonyl oxygen atoms in esters, amides, anhydrides and carbonyl oxygen atoms in hydroxyls or ethers (group 2), the ether oxygen atoms in esters and anhydrides (group 3),

and the oxygen atoms in carboxyl groups (group 4). The atomic contents of C, N and O species of NDPMC were calculated quantitatively as 84.95, 4.55, and 10.49 at%, respectively. The synergy of N-6, N-5, and N-G would contribute to the capacitance behavior of NDPMC greatly with pseudo-capacitance.

Evaluation of electrochemical performance

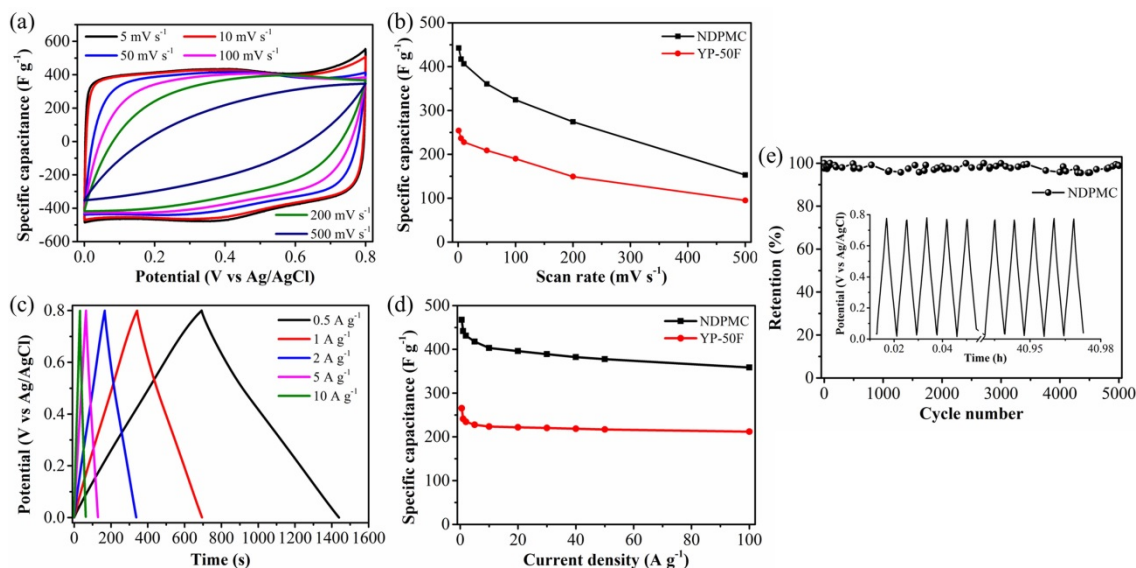


Figure 3-8. Electrochemical performance measured in the three-electrode system. CV curves of NDPMC at various scan rates from 5 to 500 mV s⁻¹ (a), Comparison of specific capacitance as a function of scan rate for NDPMC and YP-50F (b), GC curves of NDPMC at different current densities from 0.5 to 10 A g⁻¹ (c), Comparison of specific capacitance as a function of current density for NDPMC and YP-50F (d), and Capacitance retention of NDPMC at the constant current density of 20 A g⁻¹ for 5000 cycles with the first 5 and last 5 cycles inset (e).

To accurately evaluate the electrochemical performance, NDPMC as electrode was investigated by CV and GC measurements at various scan rates and current densities in a three-electrode system. For comparison, a commercial activated carbon (YP-50F, Kuraray Chemical Co.) was tested as a reference under the same condition. Fig. 3-8a showed the CV curves of NDPMC-based electrode in 1 M H₂SO₄ at different scan rates. The CV curves still maintained a satisfactory rectangular shape and no

dramatic distortions were observed at as high as 200 mV s^{-1} , indicating a typical electrical double layer capacitive behavior. Rate capability is considered as one key factor for the application of carbon-based electrode materials. Fig. 3-8b summarized the specific capacitance of NDPMC and YP-50F at a wide range of scan rates from 1 to 500 mV s^{-1} . It is well known that specific capacitance of electrode materials decreases with the increase of scan rate, which is attributed to the diffusion limitation.¹⁸ As shown in Fig. 3-8b, the capacitance retention of NDPMC exhibited as high as 62% at a scan rate of 200 mV s^{-1} from 1 mV s^{-1} , demonstrating a quick ion transport capability and excellent rate performance. Obviously, the specific capacitance calculated by Eq. 2-1 at a scan rate of 100 mV s^{-1} was 324 F g^{-1} which was much higher than that of YP-50F (188 F g^{-1}) and other electrode samples.⁷

The GC curves of NDPMC measured in $1 \text{ M H}_2\text{SO}_4$ at current densities varied from 0.5 to 10 A g^{-1} retained linearity and symmetry very well as shown in Fig. 3-8c. The typical isosceles triangular shape without obvious voltage drops (IR) revealed an indication of excellent capacitive behavior due to low internal resistance of NDPMC. It was noticed that the charge/discharge time significantly decreased with the increase of current density because the electrolyte ions had sufficient time to enter and diffuse into the porosity at relatively lower current density.¹⁹ The gravimetric specific capacitances as a function of current density were calculated by Eq. 2-2 and plotted in Fig. 3-8d, indicating the superior rate capability of NDPMC. Obviously, NDPMC displayed a larger specific capacitance than YP-50F. The specific capacitance for NDPMC was 442 F g^{-1} at 1 A g^{-1} and 359 F g^{-1} even at a very high current density of 100 A g^{-1} , resulting in a high retention rate of 81%. As a typical characteristic for electrode materials of SCs, the cycling stability of NDPMC-based electrode was carried out by the GC measurement at the constant current density of 20 A g^{-1} (Fig. 3-8e). Remarkably, the obtained carbon possessed outstanding cycle durability with a high retention rate of 98% after 5000 cycles and excellent reversibility. And the GC curves of the first five and the last five cycles were almost identical isosceles triangles, demonstrating an

outstanding long-term cycle stability of NDPMC (Fig. 3-8e, inset).

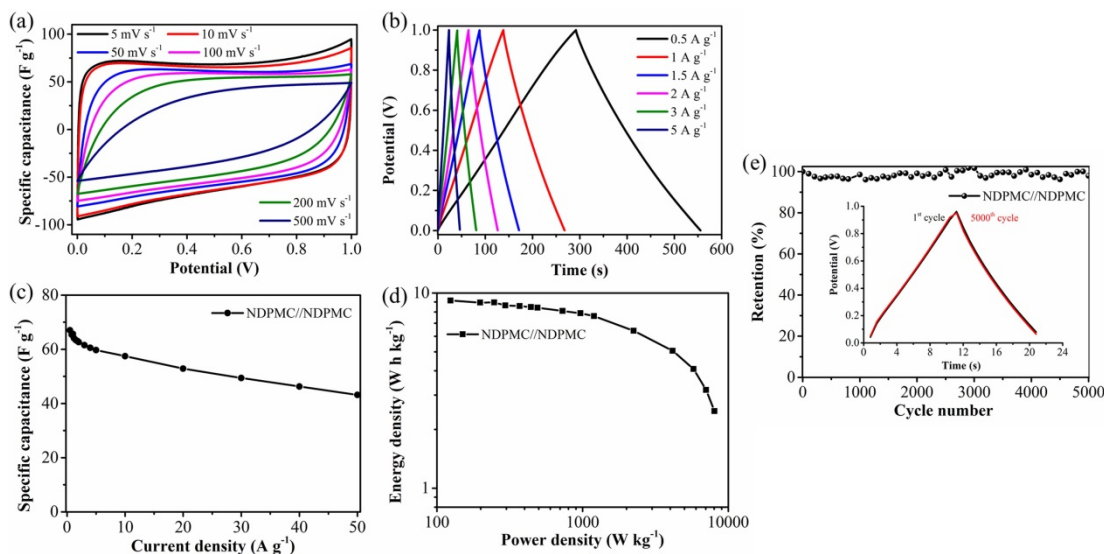


Figure 3-9. Electrochemical performance of NDPMC-based symmetric SC with a potential window of 0-1 V. CV curves at various scan rates from 5 to 500 mV s^{-1} (a), GC curves at different current densities from 0.5 to 5 A g^{-1} (b), Comparison of specific capacitance of the total SC as a function of current density (c), Ragone plot referring to energy and power density (d), and Cycle stability of NDPMC-based SC measured at the constant current density of 10 A g^{-1} with the 1st and 5000th cycles inset (e).

In order to further investigate the electrochemical capacitive practical performances, a two-electrode symmetrical SC was assembled with two nearly identical (weight and size) NDPMC films as electrodes and 1 M H_2SO_4 aqueous solution as electrolyte. The CV curves of NDPMC-based SC (Fig. 3-9a) presented a quasi-rectangular shape even at a scan rate of 200 mV s^{-1} , indicating a significant EDL capacitive behavior. Moreover, the GC curves (Fig. 3-9b) showed a linearly symmetric triangular shape within a potential window of 0-1 V, revealing high capacitive reversibility. The rate capability of NDPMC was plotted in Fig. 3-9c based on the discharge time of GC curves. The specific capacitance of the total NDPMC//NDPMC based SC was calculated as 67 F g^{-1} at 0.5 A g^{-1} by Eq. (1-1), resulting in a good rate capability of 79% at 20 A g^{-1} (Fig. 3-9c). It was noted that the specific capacitance of NDPMC reached 467 F g^{-1} at 0.5 A g^{-1} in the three-electrode system, which was much

larger than the corresponding one of 267 F g^{-1} in the two-electrode system. Generally, the asymmetry of capacitances in different potential ranges will result in a smaller capacitance in two-electrode system than that in three-electrode system for the pseudo-capacitance-based carbon materials.²⁰ While for the carbon materials based on the mechanism of electric double layer capacitance (EDLC), the capacitance usually keeps unchanged in different potential ranges, which leads to the similar performance in two-electrode system to that in three-electrode system.^{21, 22}

Table 3-2. Comparison of the porous carbons prepared in this thesis.

| Samples | S_{BET} (m^2/g) | N (%) | C_t (F/g) | | E_t (Wh/kg) | | P_t (W/kg) | |
|------------------------|---|----------|-------------|--------------|---------------|----------------|--------------|---------------|
| | | | 0.5 A/g | 20 A/g | 0.2 A/g | 20 A/g | 0.2 A/g | 20 A/g |
| ASAC (Chapter 1) | 1770 | 0.12 | 34 | 28 (5A/g) | 4.73 | 1.69 (5A/g) | 49.0 | 870 (5A/g) |
| KOH-PMC (Chapter 2) | 1600 | 5.63 | 59 | 40 | 8.42 | 2.94 | 49.7 | 3666 |
| NDPMC | 1790 | 7.96 | 67 | 53 | 9.05 | 5.06 | 49.9 | 4151 |

The existence of N-surface functional groups brought in the additional pseudo-capacitance, which generated relatively small capacitance in two-electrode system. Hence, the specific capacitances in two-electrode system were lower than those in three-electrode system. The power and energy are powerful information regarding the electrochemical performance of electrode materials, and they are estimated using GC curves. The Ragone plot represented a correlation between energy density and power density of the NDPMC-based SC, which was calculated by Eq. 1-2 and 1-3, respectively (Fig. 3-9d). The energy density in 1 M H_2SO_4 decreased from 9.2 to 5.1 Wh kg^{-1} with the increase of current density from 0.5 to 20 A g^{-1} , while power density reached to 4150 from 124 W kg^{-1} with a maximum value of 8040 W kg^{-1} at 50 A g^{-1} . The energy densities decreased slowly even with a 40-fold increase in current densities, suggesting that NDPMC is a desired electrode material for high performance SC. The cycle stability of NDPMC-based SC was evaluated by GC measurement at 10 A g^{-1} ,

exhibiting the high capacitance retention of 98% after 5000 cycles (Fig. 3-9e). In addition, the GC curves in the first and 5000th cycles were almost unchanged (Fig. 3-9e, inset). NDPMC as electrode materials presented excellent electrochemical performance in both two- and three-electrode systems in comparison with the individual ASAC and PMC (Table 3-2), demonstrating the potential application of NDPMC in practical energy storage devices. It is worth noting that NDPMC with a similar BET surface area but high N content brings in a superior electrochemical performance in comparison with ASAC and PAN-based NDPMC (Table 3-1 & 3-2), which means the introduction of nitrogen successfully enhances the capacitances of the composite carbon.

3.4 Conclusion

The author successfully obtained N-doped porous monolithic carbon from biomass-based activated carbon and PAN composite *via* a facile template-free method and its electrochemical performance for SC electrodes was investigated. The results showed that NDPMC with large surface area and high nitrogen content exhibited high specific capacitance, outstanding rate capability, and excellent cycle stability, indicating that NDPMC is a promising candidate for high performance SC. The feasible, low-cost synthetic route reported herein demonstrates great potential for large-scale production of high-performance electrode materials for SC. Furthermore, the provided route is highly possible for the production of a new class of electrode materials derived from other biomass and polymers.

3.5 References

1. Q. Wang, J. Yan and Z. Fan, *Energy Environ. Sci.*, 2016, **9**, 729-762.
2. Y. Deng, Y. Xie, K. Zou and X. Ji, *J. Mater. Chem. A*, 2016, **4**, 1144-1173.
3. Y. Zhu, S. Murali, M. D. Stoller, K. J. Ganesh, W. Cai, P. J. Ferreira, A. Pirkle, R. M. Wallace, K. A. Cychosz, M. Thommes, D. Su, E. A. Stach and R. S. Ruoff, *Science*, 2011, **332**, 1537-1541.
4. P. Chen, L. K. Wang, G. Wang, M. R. Gao, J. Ge, W. J. Yuan, Y. H. Shen, A. J. Xie and S. H. Yu, *Energy Environ. Sci.*, 2014, **7**, 4095-4103.
5. X. Zhang, L. Ma, M. Gan, G. Fu, M. Jin, Y. Lei, P. Yang and M. Yan, *J. Power Sources*, 2017, **340**, 22-31.
6. Y. Xin, Q. Xiong, Q. Bai, M. Miyamoto, C. Li, Y. Shen and H. Uyama, *Carbohydrate Polymers*, 2017, **157**, 429-437.
7. Y. Wang, B. Fugetsu, Z. Wang, W. Gong, I. Sakata, S. Morimoto, Y. Hashimoto, M. Endo, M. Dresselhaus and M. Terrones, *Sci. Rep.*, 2017, **7**, 40259.
8. S. Lei, W. Cao, Z. Fu and L. Xu, *J. Appl. Polym. Sci.*, 2016, **133**, 43890.
9. S. Faraji, M. F. Yardim, D. S. Can, A. S. Sarac, *J. Appl. Polym. Sci.*, 2017, **134**, 44381.
10. M. S. A. Rahaman, A. F. Ismail and A. Mustafa, *Polym. Degrad. Stab.*, 2007, **92**, 1421-1432.
11. A. Palanisamy, N. V. Salim, B. L. Fox, P. Jyotishkumar, T. Pradeep and N. Hameed, *RSC Adv.*, 2016, **6**, 55792-55799.
12. L. Yao, G. Yang and P. Han, *RSC Adv.*, 2016, **6**, 43748-43754.
13. J. Maruyama, T. Shinagawa, A. Hayashida, Y. Matsuo, H. Nishihara, T. Kyotani, *ChemElectroChem*, 2016, **3**, 650-657.
14. J. M. Jiménez Mateos, J. L. G. Fierro, *Surf. Interface Anal.*, 1996, **24**, 223-236.
15. J. Casanovas, J. M. Ricart, J. Rubio, F. Illas, J. M. Jiménez-Mateos, *J. Am. Chem. Soc.*, 1996, **118**, 8071-8076.

16. J. Maruyama, M. Umemura, M. Inaba, A. Tasaka, I. Abe, *J. Electrochem. Soc.*, 2009, **156**, A181-A186.
17. U. Zielke, K. J. Hüttinger, W. P. Hoffman, *Carbon*, 1996, **34**, 983-998.
18. G. Zu, J. Shen, L. Zou, F. Wang, X. Wang, Y. Zhang and X. Yao, *Carbon*, 2016, **99**, 203-211.
19. G. Ma, Q. Yang, K. Sun, H. Peng, F. Ran, X. Zhao and Z. Lei, *Bioresour. Technol.*, 2015, **197**, 137-142.
20. V. Khomenko, E. Frackowiak, F. Béguin, *Electrochim. Acta*, 2005, **50**, 2499-2506.
21. K. Xie, X. Qin, X. Wang, Y. Wang, H. Tao, Q. Wu, L. Yang, Z. Hu, *Adv. Mater.*, 2012, **24**, 347-352.
22. M. D. Stoller, R. S. Ruoff, *Energy Environ. Sci.*, 2010, **3**, 1294-1301.

Concluding remarks

As described in this doctoral thesis, porous carbons with the advantages of hierarchical structure and nitrogen doping were developed from biomass and polymer. The electrochemical application of these carbons on SCs was systematically evaluated. The results obtained through this thesis are summarized as follows.

In Chapter 1, the preparation of hierarchically porous ACs from AS through a green steam activation process and their application on the symmetric SC electrodes are described. The effect of the activation conditions on the specific surface area and porosity were explored systematically. The specific surface area and pore volume gradually increased with the enhancing of the activation temperature or the prolonging of activation time, whereas the yield of ACs showed the opposite trend. In addition, the electrochemical performances of ACs were fully evaluated on an assembled AC//AC symmetric SC system. The results revealed that AS-900-3, AC activated at 900 °C for 3 h under a steam atmosphere, possessed high specific capacitance and long cycling life, which was attributed to the relatively high surface area and proper pore size distribution.

Chapter 2 demonstrates the fabrication of N-doped porous monolithic carbons (PMC) from PAN *via* a facile template-free TIPS approach followed by an easy pyrolysis process. 3D PAN monolith was firstly fabricated as the starting material. The shape of the 3D monolith could be designed during the phase separation step, revealing the product carbons have the potential advantages of plentiful porosity and controllable shape. Two typical activation methods were employed and compared to prepare PMC. The specific surface areas and porosity parameters were systematically investigated. KOH-activated PMC showed a larger specific surface area and higher N content in comparison with that of being activated in the carbon dioxide atmosphere (CD-PMC). The electrochemical measurements were fully carried out on both three- and two-electrode systems. The results showed that PMC, possessing a large surface area, suitable pore size distribution, and high N content, displayed a high specific capacitance,

excellent cycle stability, and long cycle life.

In Chapter 3, the author successfully designs a facile route for the synthesis of N-doped porous monolithic carbon (NDPMC) from ASAC/PAN composite through the combination of template-free TIPS approach and KOH activation process. The composite monolith displayed a 3D porous structure and ASAC was found to be uniformly distributed across the PAN matrix. The 3D composite monolith showed a higher weight residue and larger specific surface area than that of pure PAN monolith. Compared to the data from ASAC (Chapter 1) and PMC (Chapter 2), the composite NDPMC possessed larger surface area and higher nitrogen content, resulting in high specific capacitance, outstanding rate capability, and excellent cycle stability. The results reveal that NDPMC is a highly promising candidate for high performance SC.

In conclusion, several kinds of porous carbons were successfully prepared from biomass and polymer. The porous carbons with high surface area, suitable pore size, and a certain amount of heteroatoms doping have been applied for high performance SC. These porous carbons will find other useful applications in various fields and contribute to the sustainable development. Furthermore, the feasible, low-cost synthetic routes for the preparation of porous carbons will be expected to extend to other types of biomass and polymer sources.

List of publications

1. Hierarchical porous carbon from greening plant shell for electric double-layer capacitor application

Yu Shu, Ayumi Dobashi, Cong Li, Yehua Shen and Hiroshi Uyama

Bulletin of the Chemical Society of Japan, 2017, **90**, 44-51.

2. Hierarchical activated green carbons from abundant biomass waste for symmetric Supercapacitors

Yu Shu, Jun Maruyama, Satoshi Iwasaki, Cong Li, Yehua Shen and Hiroshi Uyama

Bulletin of the Chemical Society of Japan, 2017, **90**, 1058-1066.

3. Fabrication of N-doped and shape-controlled porous carbons from polyacrylonitrile as electrode materials for supercapacitors

Yu Shu, Jun Maruyama, Satoshi Iwasaki, Shohei Maruyama, Yehua Shen and Hiroshi Uyama

RSC Advances, 2017, **7**, 43172-43180.

4. Nitrogen-doped biomass/polymer composite porous carbon for high performance supercapacitor

Yu Shu, Jun Maruyama, Satoshi Iwasaki, Shohei Maruyama, Yehua Shen and Hiroshi Uyama

Journal of Power Sources, 2017, **364**, 374-382.

List of supplementary publication

1. Activated carbon monolith derived from *Amygdalus pedunculata* shell and polyacrylonitrile for supercapacitors

Yu Shu, Jun Maruyama, Satoshi Iwasaki, Yehua Shen and Hiroshi Uyama

Bulletin of the Chemical Society of Japan, accepted.

Acknowledgments

This study was carried out from 2014 to 2017 at the Department of Applied Chemistry, Graduate School of Engineering, Osaka University. Completing the PhD is the most fantastic experience in my whole life and successfully achieving the great goal depends on the countless assistance and support from all members around me over the past three years.

First and foremost, I would like to express my deepest gratitude to my supervisor, Prof. Hiroshi Uyama, for the excellent supervision, constant guidance, invaluable discussion, and kindhearted encouragement throughout this whole work. Discussing with him can always broaden my vision and bring useful ideas to the research. His keen and vigorous academic observation enlightens me not only in this thesis but also in my future study. I also want to thank him for providing me with the chance to study at Osaka University as an exchange student from September 2013 to May 2014. The precious experience greatly inspired my academic interest and promoted me to make up my mind to pursue the doctoral study.

I am profoundly grateful to Dr. Jun Maruyama, Environmental Technology Research Division, Osaka Municipal Technical Research Institute, for his efforts and enthusiasm in knowledge sharing and manuscripts revising. And I also would like to thank Dr. Satoshi Iwasaki and Dr. Shohei Maruyama for the experimental operation and data discussion.

I would like to express great thanks to Prof. Susumu Kuwabata and Prof. Nobuhito Imanaka for their valuable comments and suggestions on preparation of this thesis.

I am especially grateful to Assistant Prof. Takashi Tsujimoto and Associated Prof. Taka-aki Asoh for their kind help and expert advises.

I also appreciate the help from Assistant Prof. Taro Uematsu for the TEM measurement, and Associated Prof. Shinji Tamura for the XRD measurement.

I am much indebted to Prof. Yehua Shen, College of Chemistry and Materials

Science, Northwest University, for her continuous encouragement and support to pursue my doctoral degree overseas. And I also give my sincere thanks to Dr. Cong Li for her helpful suggestions and heartfelt supports.

I am very thankful to the past and present fellow labmates in Uyama laboratory, Dr. Yuanrong Xin, Dr. Xiaoxia Sun, Dr. Wenjuan Han, Dr. Guowei Wang, Dr. Boxing Zhang, Dr. Tengjiao Wang, Dr. Hyunhee Shim, Mr. Mononari Kanno, Mr. Qidong Wang, Ms. Zhaohang Yang, Ms. Ayumi Dobashi, Mr. Kenta Chashiro, Mr. Keng Yao Tan, Ms. Jingyuan Niu, Ms. Xingyu Xiang, Mr. Jia Yu Chen, Ms. Hoi I Neng, Ms. Jin Qian, etc. for their kind help, assistance, and friendship which makes my PhD studies easier and fruitful.

I wish to appreciate the kind help and warm-hearted support from Ms. Yoko Uenishi and Ms. Tomoko Shimizu.

The financial support from China Scholarship Council (CSC) for my academic training studies and my stay in Japan is greatly appreciated.

Last but not least, I would like to express particular appreciation to my parents, Xiacheng Shu and Yuexia Wang, and my husband, Shengjie Zhang for their endless love, motivation, and encouragement in my life.

August 2017

Yu Shu